MICRO LOOP HEAT PIPE EVAPORATOR COHERENT PORE STRUCTURES

A Thesis

by

ALEXANDRE VIKTOROVICH ALEXSEEV

Submitted to the Office of Graduate Studies of
Texas A&M University
in partial fulfillment of the requirements for the degree of

MASTER OF SCIENCE

August 2003

Major Subject: Nuclear Engineering

MICRO LOOP HEAT PIPE EVAPORATOR COHERENT PORE STRUCTURES

A Thesis

by

ALEXANDRE VIKTOROVICH ALEXSEEV

Submitted to Texas A&M University
in partial fulfillment of the requirements
for the degree of

MASTER OF SCIENCE

Approved as to style and content by:

<div style="display:flex; justify-content:space-between;">

Frederick R. Best
(Chair of Committee)

Yassin A. Hassan
(Member)

</div>

<div style="display:flex; justify-content:space-between;">

Gerald L. Morrison
(Member)

William E. Burchill
(Head of Department)

</div>

August 2003

Major Subject: Nuclear Engineering

ABSTRACT

Micro Loop Heat Pipe Evaporator Coherent Pore Structures. (August 2003)

Alexandre Viktorovich Alexseev, B.S., Obninsk Institute of Nuclear Power Engineering

Chair of Advisory Committee: Dr. Frederick Best

Loop heat pipes seem a promising approach for application in modern technologies where such thermal devices as cooling fans and radiators cannot satisfy overall requirements. Even though a loop heat pipe has a big potential to remove the thermal energy from a high heat flux source, the heat removal performance of heat pipes cannot be predicted well since a first principles of evaporation has not been established. An evaporation model based on statistical rate theory has been recently suggested by Ward[1] and developed for a single pore by Oinuma.[2] A loop heat pipe with coherent pore wick structure has been proposed as a design model.

To limit product development risk and to enhance performance assurance, design model features and performance parameters have been carefully reviewed during the concept development phase and have been deliberately selected so as to be well-founded on the limited existing loop heat pipe knowledge base. A first principles evaporation model has been applied for evaporator geometry optimization. A number of iteration calculations have been performed to satisfy design and operating limitations. A set of recommendations for design optimization has been formulated. An optimal model has been found and proposed for manufacture and experimental investigation.

ACKNOWLEDGEMENTS

TABLE OF CONTENTS

LIST OF TABLES

LIST OF FIGURES

NOMENCLATURE

Symbol	Description
A	Hamaker constant (J) or empirical constant
A_{evap}	Evaporation area (m^2)
A_{pore}	Pore cross sectional area (m^2)
$A_{tr\ line}$	Transport line cross-sectional area (m^2)
B	Empirical constant
Bi	Biot number
C	Empirical constant
C_f	Fanning friction factor
C_n	Tabulated coefficient
C_p	Specific heat at constant pressure (J/kg K)
D	Empirical constant
$\dot{E}_{in}$	Inlet energy per unit time (J/s)
$\dot{E}_{out}$	Outlet energy per unit time (J/s)
ER	Evaporation rate (kg/s m^2)
Fo	Fourier number
Jo	Zero order Bessel function
L	Length (m)

M	Working fluid molecular weight (kg)
N_A	Avogadro's number (molecules/mol)
N_{pore}	Total pore number
P	Pressure (Pa)
P_l	Liquid pressure (Pa)
$P_{sat}(T_l)$	Saturation pressure at liquid temperature for flat interface
P_v	Vapor pressure (Pa)
$P_\infty(T_l)$	Saturation pressure at liquid temperature for curved interface (Pa)
R	Radius (m)
R_c	Radius of curvature (m)
Re	Reynolds number
$Re_v^{tr\ line}$	Vapor transport line Reynolds number
$Re_v^{channel}$	Vapor channel Reynolds number
T	Temperature (K)
T_b	Post bottom temperature (K)
T_{chip}	Chip surface temperature (K)
T_{cl}	Centerline temperature (K)
T_i	Initial temperature (K)
T_{li}	Interfacial liquid temperature (K)

T_{sat}	Saturation temperature (K)
T_t	Post top temperature (K)
T_{vi}	Interfacial vapor temperature (K)
T_w	Pore wall temperature (K)
V	Velocity (m/sec)
$V_V^{tr\ line}$	Transport line vapor velocity (m/sec)
W	Unit cell width (m)
X	Coordinate direction
Y	Coordinate direction
b	Post bottom width (m)
c	Post width at any post height (m)
d	Diameter (m)
$d_{tr\ line}$	Transport line diameter (m)
$d_V^{channel}$	Vapor channel hydraulic diameter (m)
f	Darcy friction factor
h	Post height (m)
h_{fg}	Latent heat of vaporization (J/kg)
k	Boltzmann's constant (J/ K molecule)
k	Thermal conductivity (W/m K)
k_l	Liquid thermal conductivity (W/m K)

m	Working fluid atomic mass (kg/mol)
$\dot{m}$	Evaporation rate (kg/sec m^2) or mass flow rate (kg/sec)
$\dot{m}_{total}$	Total mass flow rate (kg/sec)
p	Pitch (m)
q_{vib}	Vibrational partion function
q_x	Heat transfer rate in X direction (W)
$q"$	Heat flux (W/m^2)
$q"_{chip}$	Chip heat flux (W/m^2)
$q"_{pore}$	Pore heat flux (W/m^2)
r	Spatial coordinate (m)
$r*$	Dimensionless spatial coordinate
t	Evaporator thickness (m) or time (sec)
ΔP_c	Capillary pressure rise (Pa)
ΔP_l	Liquid pressure drop (Pa)
ΔP_v	Vapor pressure drop (Pa)
ΔS	Entropy difference between liquid and vapor (J/kg K)
ΔT_{pore}	Temperature difference between vapor channel center pore and closest to the post pore (K)
ΔT_{post}	Temperature difference between post top and bottom (K)
$\Delta T_{structure}$	Temperature difference between temperature under the post and maximal evaporator backside temperature (K)

Θ	Vibrational characteristic temperature (K)
α	Thermal diffusivity (m^2/sec)
δ	Liquid film thickness (m)
ζ	Tabulated coefficient
θ	Contact angle
ϑ_0^*	Dimensionless centerline temperature
μ	Absolute viscosity (Pa s)
μ_v	Vapor chemical potential (J/kg molecule) or vapor viscosity (Pa s)
ν_l	Liquid kinematic viscosity, (m^2/s)
ρ	Density (kg/m^3)
ρ_v	Vapor density (kg/m^3)
σ	Surface tension (N/m)

CHAPTER I

INTRODUCTION AND DESIGN CONCEPT

INTRODUCTION

The problem of heat transfer between source and sink is as old as life. However, this is a special issue for modern technologies such as Nuclear Engineering, Electronics, Space Technology, and Fundamental Research. Here one can see the tension between mass and volume parameters of devices which produce thermal energy as a side effect of operation and heat transfer devices. For example cooling fan size and mass significantly exceeds those of microprocessor. Spacecraft design requirements such as low weight, low volume, and temperature control under variable heat loads and/or heat sink impose further system restrictions. Using classical thermal devices such as cooling fans and radiators cannot satisfy advanced requirements. Developing new cooling techniques is a necessity. Loop heat pipes seem to be a promising approach which can satisfy modern restrictions.

_____

This thesis follows the style and format of *Fusion Science and Technology*.

BACKGROUND

This chapter introduces the work and provides a review of existing heat pipe types along with a new design concept model.

Heat pipe technology has been under active development for the last thirty years, nevertheless an initial heat pipe concept can be found in the patents of A. M. Perkins and J. Perkins dated by the mid-1800s, and described by Peterson.[3] Having smaller weight for the same temperature difference, heat pipes are able to transfer up to thousands of times more thermal energy than copper or silver solid conductors of the same dimensions.

A conventional heat pipe, shown in Figure 1.1 is a hermetically sealed cylinder with a capillary wicking structure covering the internal walls. The wick, usually relatively thin, is saturated by liquid. The internal volume is filled by vapor and serves as a vapor transport channel. Liquid evaporates at the hot end of the heat pipe, picking up energy, associated with the latent heat of vaporization. Pressure rises at the hot end due to the evaporation process. At the same time pressure at the cold end declines due to condensation. Since pressure at the cold end is lower, vapor flows to the cold end and condenses, giving up the latent heat of vaporization. Liquid depletion at the evaporation section causes meniscus formation in the wick. Associated capillary pressure drives liquid movement from the condenser to the evaporator section through the wick. Thus a heat pipe works on the closed two phase cycle principle. Vapor velocity usually considerably exceeds liquid velocity in the wick. The wick serves as a capillary pump,

providing working fluid circulation. Its geometry and thermal characteristics highly influence overall heat pipe performance. High heat transfer capability is achieved by utilizing two opposite phase changes for fluid with high latent heat, wherein the heat transfer coefficient of phase change is normally 10-1000 times larger than typical heat transfer coefficients for conduction and forced convection.
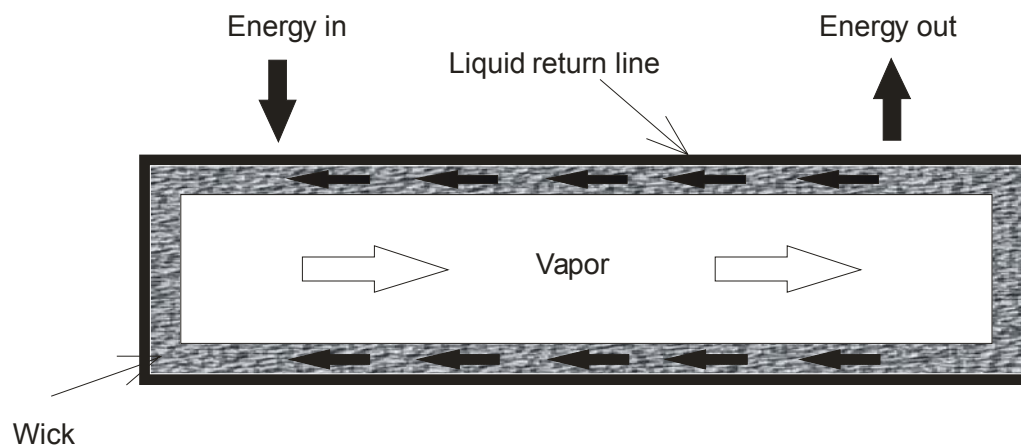
Figure 1.1. Conventional heat pipe

Gravitational forces can act codirectionally to capillary forces for a vertically oriented heat pipe with the hot end at the bottom. In this case, the gravitational force is able to provide liquid return to the evaporator without a wick structure. A heat pipe without a wick is called a thermosyphon. Gravitational forces can cause evaporator dryout for a vertically oriented heat pipe with the hot end at the top. In this case capillary forces must "pump" the liquid against gravity from the evaporator to condenser. When capillary pressure is not sufficient to provide liquid return to evaporator, the heat pipe

reaches its capillary limit and evaporator dryout occurs. The capillary limit can be increased by using a smaller pore wick structure; however this is not efficient, since liquid pressure drop also increases. Thermal energy can not be transferred a considerable distance using classical heat pipes due to liquid pressure drop in the wick.

Performance dependent on the local gravitational field and flow losses in the wick are the main disadvantages of the classical heat pipe, limiting heat pipe applications.

In a capillary pumped loop, shown in Figure 1.2.a an alternative approach has been applied.
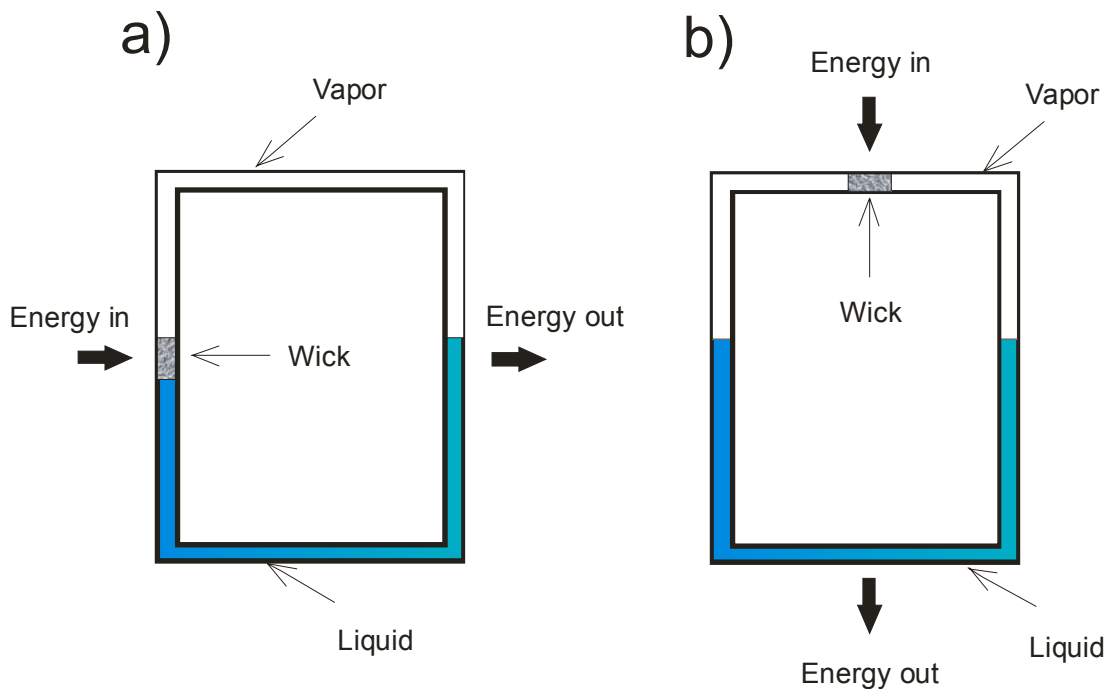
Figure 1.2. a) Capillary pumped loop; b) Deprimed capillary pumped loop

Wick size is noticeably smaller compared to a conventional heat pipe. A wick structure with significantly smaller pores can be used to achieve a capillary pressure rise of tens of kilopascals. Simple tubes can be used as liquid and vapor lines with relatively small associated pressure drop. Therefore a capillary pumped loop is able to operate against gravity at any gravitational orientation.

Figure 1.2.b shows a situation when a capillary pumped loop is deprimed and cannot start up without intervention, the wick being vapor bound. Difficult start up is a disadvantage of a capillary pumped loop compared with a conventional fully wicked heat pipe.

Heat pipes and capillary pumped loops are potentially excellent heat transfer devices. Nevertheless, associated operating requirements limit their applications. Further capability is possible using loop heat pipes.

Loop heat pipes (LHP) combine positive features of capillary pumped loops and eliminate start up difficulties by providing liquid at the wick at any space orientation and gravitational field. Maidanik's patented loop heat pipe, described by Ernst et al.,[4] is shown in Figure 1.3. Energy enters the evaporator and vaporizes working fluid at the wick surface. Vapor flows to the condenser through the system of vapor lines, designed to minimize vapor flow pressure drop. The condenser has a small annulus for condensate collection. Annulus design ensures stable operation due to gravity and/or capillary forces. Vapor pressure forces condensate to the evaporator, where condensate feeds the wick through the liquid annulus. A loop heat pipe is made self-priming by careful reservoir design, condenser, vapor pipe and liquid return pipe volume design and

proper heat load positioning during operation. Proper heat load design results in lower reservoir temperature compared to wick vapor side so that during startup initial evaporation occurs in the vapor pass rather than in liquid line or reservoirs. This ensures proper startup from any state thus making the LHP inherently self priming.
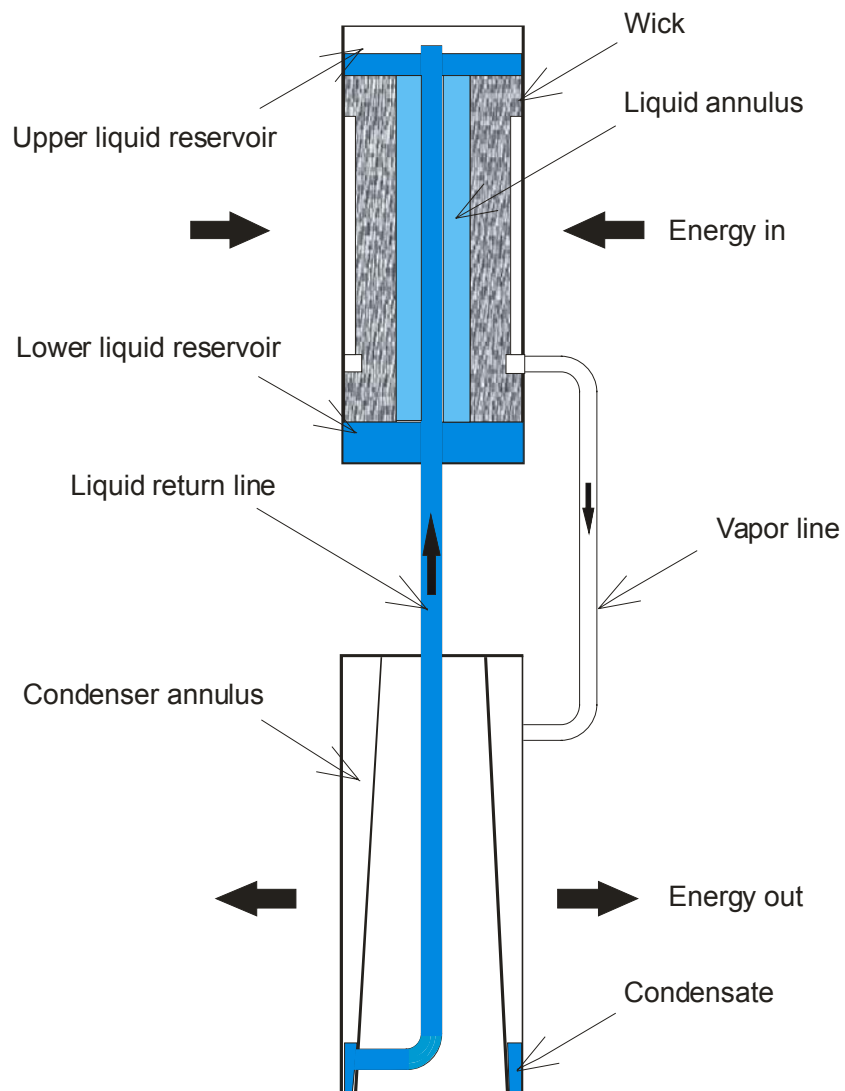
Figure 1.3. Loop heat pipe

Even though a loop heat pipe has a big potential to remove thermal energy from a high heat flux source, the heat removal performance of heat pipes cannot be predicted well since a first principles evaporation model has not been established. General loop heat pipe design is based on experimental data rather than analytical models. Sintered powdered metal, a commonly used wicking material, has a stochastic pore structure, which makes analytical or numerical calculation methods inapplicable for design optimization. Many cases have been reported by Richter and Gottschlich[5] when actual heat pipe operational parameters were different from the predicted, sometimes this difference achieved an order of magnitude range.

DESIGN CONCEPT

Design parameters were set as follows: chip heat flux in the 100's W/cm^2 range, maximal wick wall temperature – 373.15 K (100°C), chip heat transfer area $1.0*10^{-4}$ m^2 (1 cm^2). Water is the working fluid.

A loop heat pipe using a coherent pore wick structure has been proposed as a design model. An evaporation model based on statistical rate theory has been recently suggested by Ward.[1] This model called a first principles evaporation model (FPEM) has been applied by Oinuma[2] to calculate the evaporation rate for coherent pores. Evaporator fabrication is performed by using photo lithographic fabrication technology (Hamdan et al[6]). Using a coherent pore wick structure allows consideration of operating parameters at the design stage. This gives the opportunity for design optimization.

General loop heat pipe principles have been applied in the present work for a conceptual design. Main goals were achieving high heat fluxes (in 100 W/cm^2 range) and inherently passive operation. The evaporator shown in Figure 1.4 operates as follows. Thermal energy from the heat source is transferred by conduction through the posts to the evaporator. Energy is removed by evaporation of the working fluid in the pores. The conducting post and evaporator are made of silicon. Pressure forces the vapor to the condenser (not shown), from where it returns and feeds the wick. Energy may be transferred by conduction to the back side liquid reservoir, where undesirable boiling can occur. Silicon dioxide may be used at the backside of the evaporator to minimize heat transfer. Backside boiling prediction has been performed using the first principles evaporation model described in Chapter II.
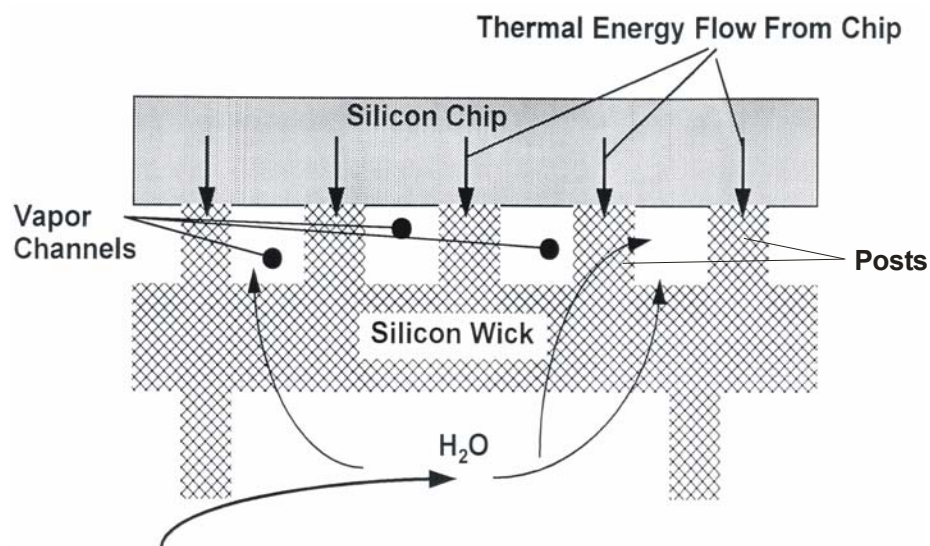
Figure 1.4. Conceptual LHP evaporator design

THESIS OUTLINE

The first part of this work, Chapter II, describes first principles evaporation model and its approximation for engineering calculations. Chapter III presents the concept design analytical model and application of the first principles evaporation model to design optimization. Chapter IV presents numerical models used to verify analytical model calculation results and to perform calculations where the analytical model was found inapplicable. Chapter V represents final design which summarizes results obtained in Chapters III and IV. Chapter VI presents a summary and conclusion of the work along with recommendations for future work.

CHAPTER SUMMARY

The major heat pipe types along with difficulties and limitations associated with their operation were described in this chapter. The intent of this description was to familiarize the reader with current heat pipe technology and show the necessity for further heat pipe development. A proposed new design concept model and desired operating parameters has been introduced.

CHAPTER II

FIRST PRINCIPLES EVAPORATION MODEL

INTRODUCTION

This chapter briefly introduces the first principles evaporation model (FPEM) and describes the studies performed to simplify the model for engineering calculations.

Figure 2.1 represents a micron scale pore wick evaporation region for which the first principles evaporation model was developed by Oinuma.[2]
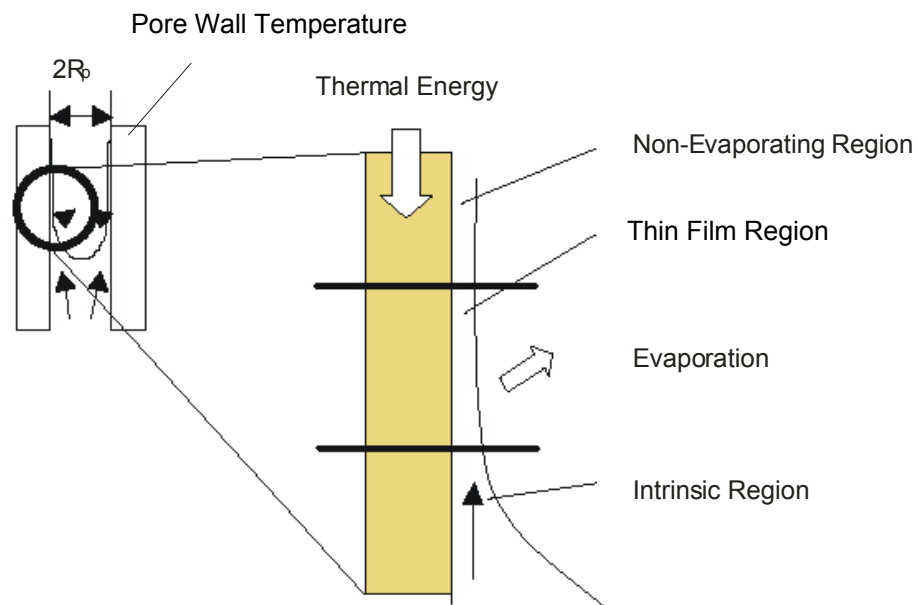
Figure 2.1. FPEM evaporation region

One can see that the meniscus, formed in the pore, is divided into three regions: non-evaporating region, thin film region and intrinsic region. The intermolecular dispersion force, also known as the disjoining pressure and Van der Waals force, between liquid molecules and wall molecules is strong enough to prevent evaporation from the liquid-vapor interface in the non-evaporating region. The intermolecular force is significantly smaller in the thin film region, where maximum evaporation occurs. The liquid thickness of this region is about the order of nano-meter. Intrinsic region evaporation rate is smaller compare to thin film region due to dominant surface tension.

See Oinuma[2] for a complete discussion of the FPEM. Briefly, however, the model is given by Equations 2.1-2.4.

$$\dot{m} = \frac{M}{N_A} \frac{P_\infty(T_{li})}{\sqrt{2mkT_{li}}} \left\{ \exp\frac{\Delta S}{k} - \exp\frac{-\Delta S}{k} \right\} \tag{2.1}$$

$$\frac{\Delta S}{k} = 4\left(1 - \frac{T_{vi}}{T_{li}}\right) + \left(\frac{1}{T_{vi}} - \frac{1}{T_{li}}\right) \sum_{l=1}^{3}\left(\frac{\Theta_l}{2} + \frac{\Theta_l}{\exp(\Theta_l/T_{vi})-1}\right) + \frac{v_l}{kT_{li}}\left(P_v - \frac{2\sigma}{R_c} - P_{sat}(T_{li}) - \frac{A}{\delta^3}\right)$$
$$+ \ln\left[\left(\frac{T_{vi}}{T_{li}}\right)^4 \frac{P_{sat}(T_{li})}{P_v}\right] + \ln\left(\frac{q_{vib}(T_{vi})}{q_{vib}(T_{li})}\right) \tag{2.2}$$

$$T_{li} = T_w - \frac{\dot{m}h_{fg}\delta}{k_l} \tag{2.3}$$

$$q_{vib}(T) = \prod_{l=1}^{3} \frac{\exp(-\Theta_l/2T)}{1-\exp(-\Theta_l/T)} \qquad (2.4)$$

where $\dot{m}$ is evaporation rate, M is working fluid molecular weight, N_A is Avogadro's number, T_{li} is interfacial liquid temperature, $P_\infty(T_l)$ is saturation pressure at liquid temperature for curved interface, m is working fluid atomic mass, k is Boltzmann constant, ΔS is entropy difference between liquid and vapor, T_{vi} is interfacial vapor temperature, Θ_l is the vibrational characteristic temperatures which are 2290, 5160 and 5360 K for water, P_v is vapor pressure, σ is surface tension, R_c is the radius of curvature, $P_{sat}(T_l)$ is water saturation pressure at liquid temperature for flat interface, A is Hamaker constant, δ is liquid film thickness, $q_{vib}(T)$ is the vibrational partion function, T_w is pore wall temperature, h_{fg} is water latent heat of vaporization, k_l is liquid conductivity.

The FPEM was developed by Ward[1] and applied by Oinuma[2] in order to eliminate the need for empirical constants required by Kinetic theory evaporation/condensation models. The FPEM can be used to calculate local evaporation as a function of local conditions i.e. at the micron scale, as well as predict wick liquid boiling, a major unresolved question for all wicked heat pipes. However, the first principles approach comes at the cost of significant complexity.

One can see that FPEM includes a number of parameters, nevertheless all parameters can be divided into three categories: constants, water thermophysical properties, and variables. Constant values are presented in Appendix 1. All water

thermophysical properties have been calculated using a FORTRAN program, developed by ASME.[7] Variables are T_w, T_{li}, T_{vi}, P_v, R_c. Liquid and vapor interfacial temperatures are parameters which are hard, if not impossible, to measure in real life. A sensitivity analysis has been performed to define their importance and simplify the overall model. Water thermophysical properties are not considered as variables and therefore are not included in sensitivity study.

SENSITIVITY STUDY

An analysis has been performed to evaluate how liquid and vapor interfacial temperatures affect the calculated evaporation rate. The above discussion shows that evaporation rate is dependent on evaporation region temperature, vapor pressure, water properties and pore diameter. The evaporation region temperature is described by three temperatures – vapor and liquid interface temperatures, and pore wall temperature. Temperature differences between them are small due to the small structure dimensions. Temperature differences between vapor temperature and pore wall temperature, and liquid temperature and pore wall temperature have been tested to evaluate the effect on evaporation rate.

Vapor collects thermal energy from the post walls (see Figure 1.4) therefore its temperature is higher than pore wall temperature. Interface vapor temperature is higher than pore wall temperature due to above effect. (This was also proved by numerical calculation, described in Chapter IV) The evaporation rate has been calculated for a

range of vapor temperatures, exceeding pore wall temperature by 5, 10, 15 and 20 degrees K and compared to the case where vapor temperature was equal to wall temperature. Comparison has been made using relative error concept, where error was calculated using Equation 2.5.

$$error_i = \frac{ER_b - ER_i}{ER_b}100\% \tag{2.5}$$

where ER_b is base evaporation rate calculated for the case with no difference between vapor and wall temperatures; ER_i is the evaporation rate calculated for any case where vapor temperature is different from wall temperature. Figures 2.2 and 2.3 present calculated error as a function of evaporation rate for different pore diameters. One can see that the error exceeds 5% in the narrow region, correspondent to small evaporation rate values and high temperature difference. Maximal evaporation rate (circled in the Figures 2.2 and 2.3) exceed those values in operating regime and error is lower for smaller diameter pore. Further calculations showed insignificant temperature difference between vapor temperature and pore wall temperature considerably lower than 5 degrees K. Therefore evaporation model can be considered independent of vapor temperature in the range of interest.
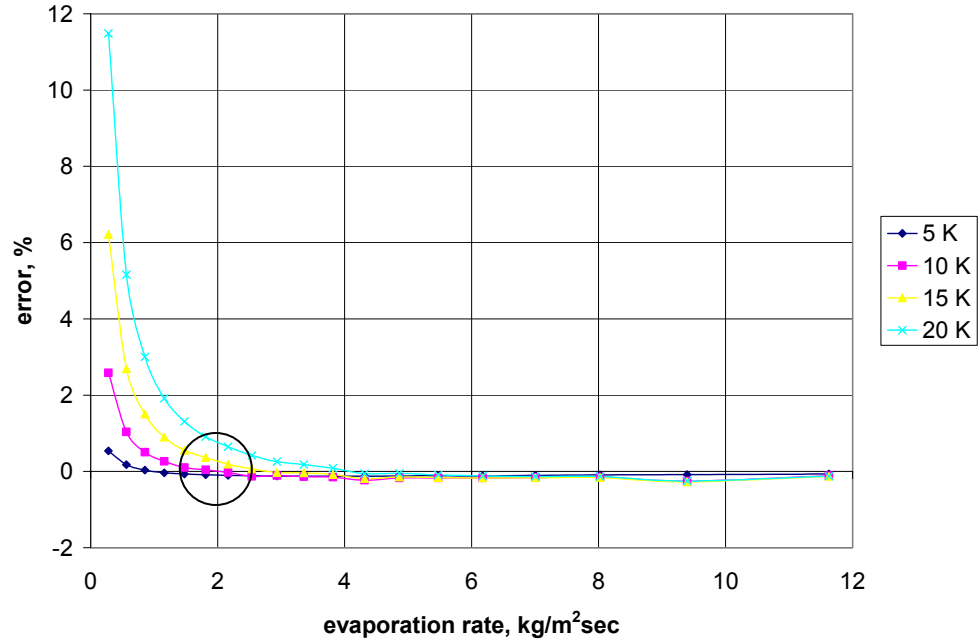
Figure 2.2. Pore evaporation rate calculation errors (10 µm diameter pore)
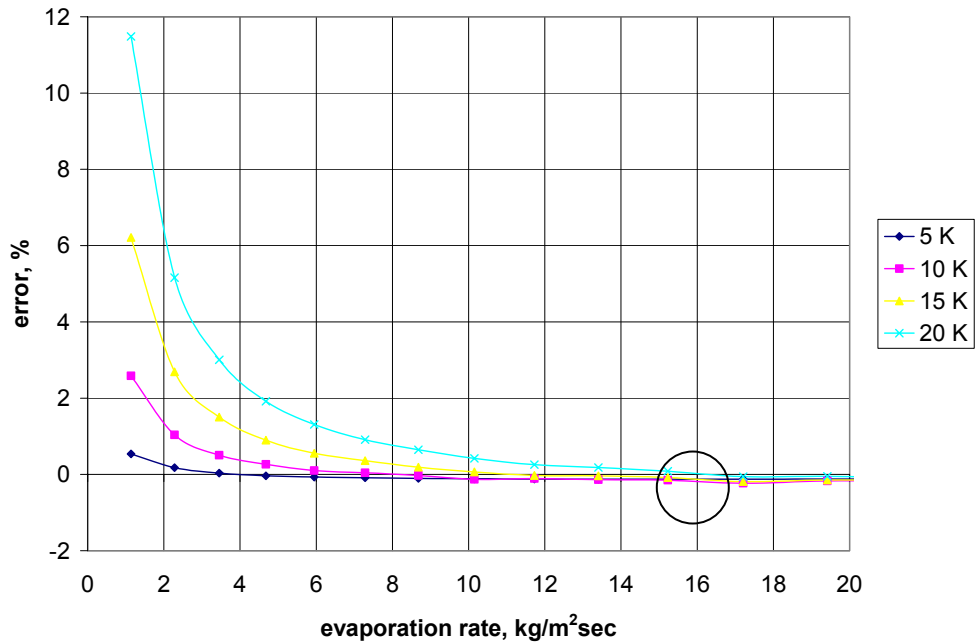
Figure 2.3. Pore evaporation rate calculation errors (1 µm diameter pore)

The interface liquid temperature was studied using a single pore of 10 μm diameter with surrounding structure; pitch to diameter ratio is 1.5, where pitch is the distance between neighbor pore centers. The following conditions have been applied: structure constant temperature boundary 373.15 K (100°C), water inlet speed 1.5*10^{-3} m/sec, water inlet temperature 363.15 K (90°C). The above parameters have been chosen on the basis of heat pipe operating conditions. Loop heat pipe operation is based on phase change and the desire for near isothermal operation. Therefore a significant difference between maximal evaporator and minimal condenser temperatures must be avoided. It has been assumed that 10 K is maximal allowed temperature difference. Although temperature differences significantly exceeding 10 K have been found from analytical and numerical modeling, described in the following chapters, the 10 K difference exceeds that for all pipes considered as viable designs.

Results of numerical model calculations for fluid temperature versus position are shown in Figure 2.4 where all coordinate map sizes are in microns, temperatures are in degrees K. Distance, starting from the water inlet at the bottom of the model to the point where the fluid has the same temperature as surrounding structure (heating length) is less than one pore diameter. Real pore profile, shown in Figure 2.1, is different from calculated geometry. Liquid film thickness in the thin film region is significantly lower compare to pore radius (nano meters compare to microns), therefore heating length is expected to be significantly smaller. Liquid film thickness in intrinsic region decreases from pore radius at the meniscus bottom to nano meters at the region top. Therefore

heating length is also expected to be smaller than calculated. Thus interface liquid temperature can be assumed equal to pore wall temperature.
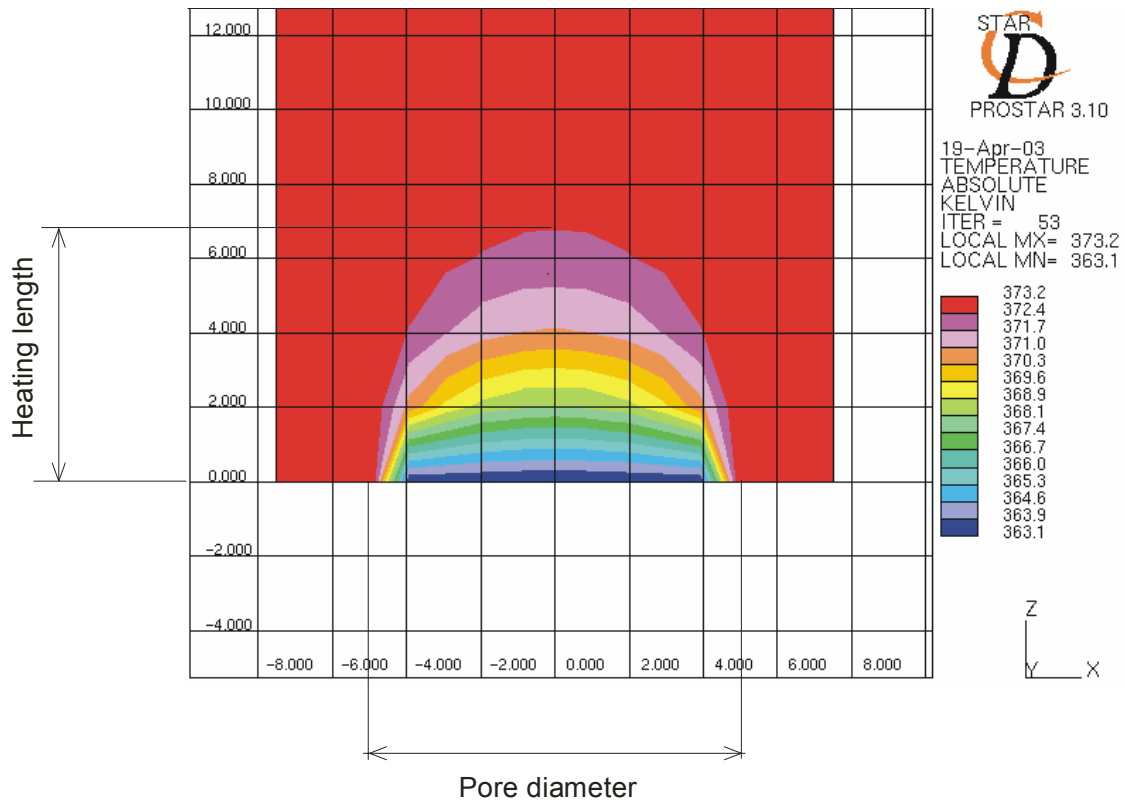
Figure 2.4. Numerical model result

Thus in spite liquid temperature and vapor temperature in the meniscus region affect total result, error in case of their approximation is small. Further calculations were performed assuming liquid and vapor interface temperatures equal to pore wall temperature.

SIMPLIFIED MODEL RESULTS

Figures 2.5 and 2.6 show the evaporation rate for 10 μm and 1 μm pores as a function of wall temperature and vapor pressure. Note that a smaller diameter pore achieves a significantly higher evaporation rate. The evaporation rate increases with lower vapor pressure and higher wall temperature, as expected.
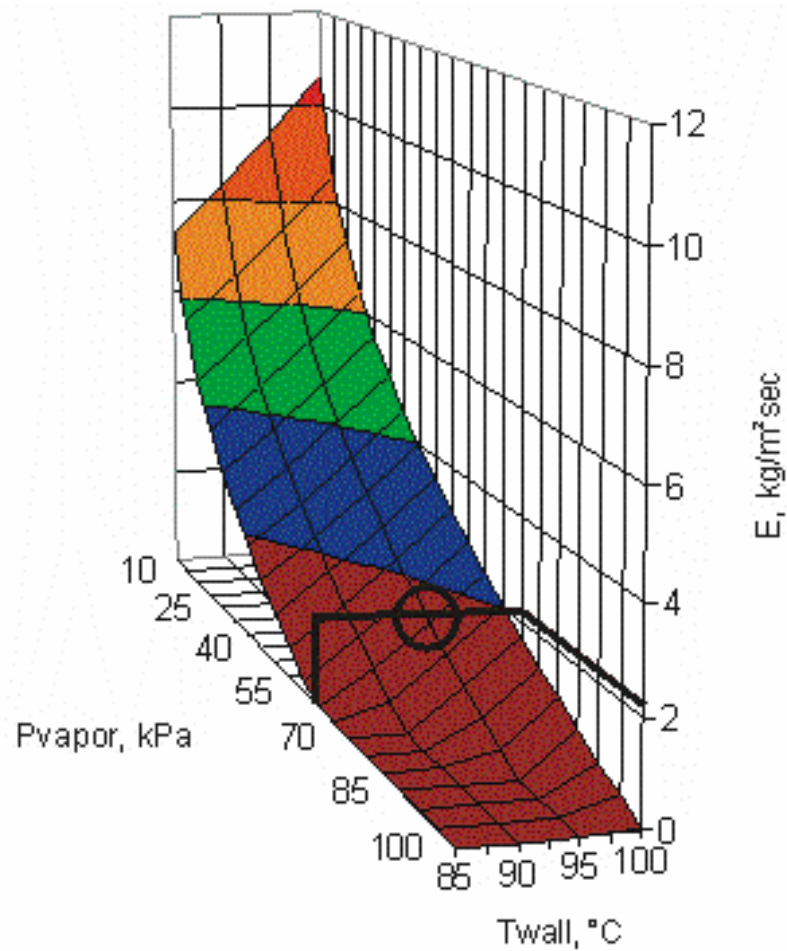
Figure 2.5. 10 μm diameter pore evaporation rate
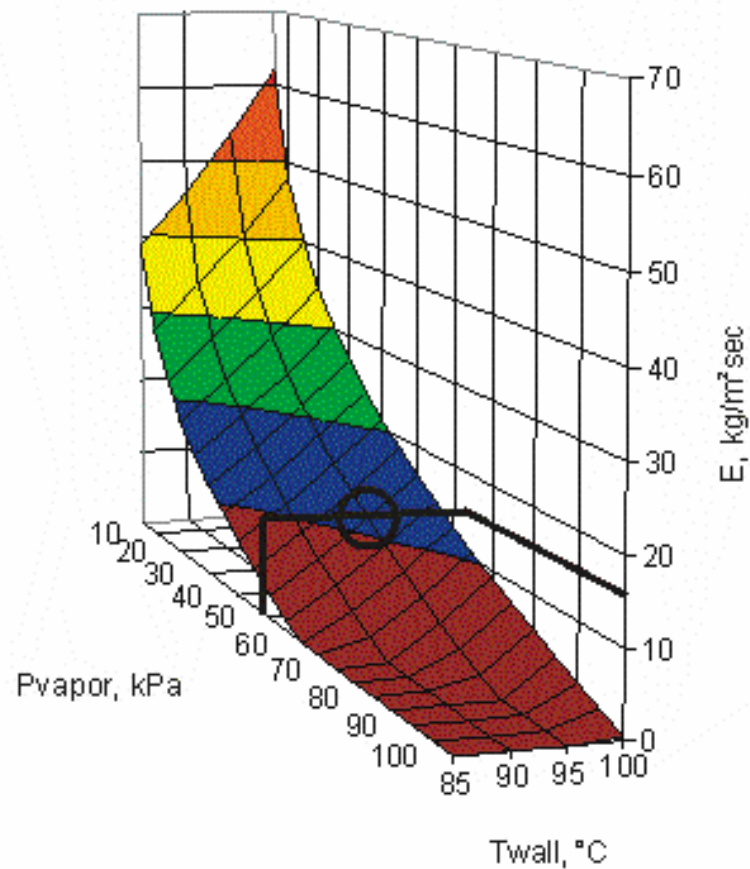
Figure 2.6. 1 μm diameter pore evaporation rate

A higher wall temperature leads to a higher liquid temperature and therefore a higher evaporation rate. Lower vapor pressure leads to lower vapor saturation temperature and therefore an increased evaporation rate.

Realizing that since total difference between pore wall temperature and water inlet temperature must be less than 10 K (10^oC), Figures 2.5, 2.6 and 2.7 set maximum upper limits of the evaporation rate for 1 and 10 μm diameter pores. Maximum evaporating rate was found as follows. Pore wall temperature is lower than wick wall

temperature, set to 373.15 K (100°C) by design limitation, by post temperature drop. Maximal post temperature drop is about 5 K, as it was calculated using one dimensional heat conduction post model for geometries presented in Chapter III. Therefore minimal pore wall temperature is 368.15 K (95°C). Maximal evaporator temperature is equal to pore wall temperature and is 368.15 K (95°C) for geometry with maximal post temperature drop. Minimal condenser temperature is 358.15 K (85°C) for the same geometry. Vapor pressure maximal value is equal to saturation pressure for evaporator temperature. Minimal value can be roughly assumed to be equal to saturation pressure for condenser temperature, neglecting transport line vapor pressure drop. Figure 2.7 shows water saturation pressure for the temperatures range of interest. One can see that minimal vapor pressure is about 58 kPa.
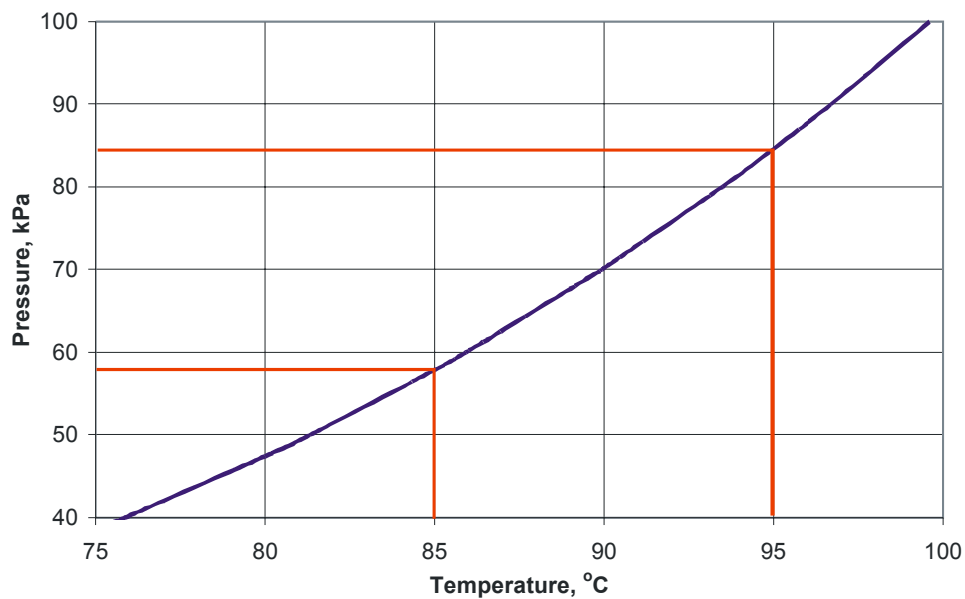
Figure 2.7. Saturation pressure as a function of temperature

Maximal evaporation rates of about 2 kg/m^{2}sec and 16 kg/m^{2}sec have been found (circled in Figures 2.5 and 2.6) for 10 µm and 1 µm pore diameters correspondingly, using above vapor pressure value and pore wall temperature of 368.15 K (95°C).

The evaporation rate can also be expressed in terms of the heat flux which represents the pore heat removal capability. Values for pore diameters of 10 µm and 1µm are shown in Figures 2.8 and 2.9. It is this heat flux which is used for the macroscopic design of the evaporator wick, i.e. how the pore effective (evaporation) heat flux varies as wall temperature and vapor pressure vary. This design process is described in Chapter IV.
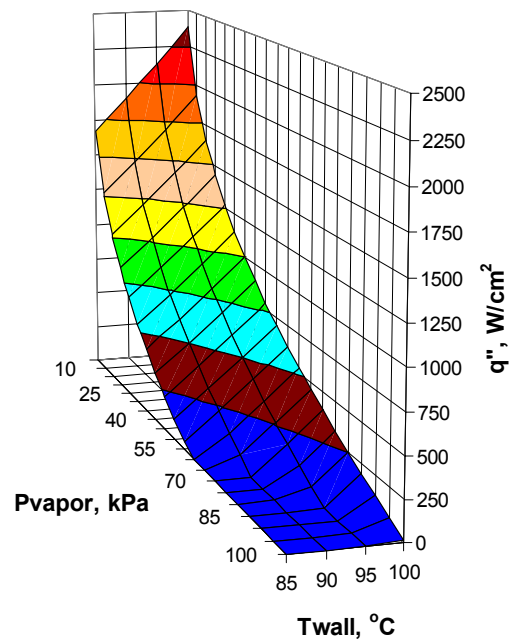
Figure 2.8. 10 µm diameter pore heat removal capability
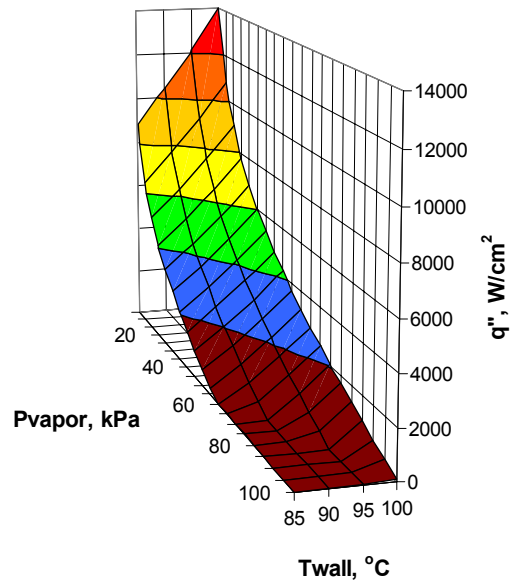
Figure 2.9. 1 μm diameter pore heat removal capability

The boundary condition at the pore top as a function of the heat flux from wall temperature for a number of vapor pressure values has been found and applied in a numerical model calculation, described in Chapter IV to calculate evaporator temperature distribution.

Equation 2.6 represents an example of an empirical fit of a pore heat flux as a function of pore wall temperature and vapor pressure for a pore diameter

$$q_{pore}^{"} = \frac{(A + T_w)}{(B + CP_v)} + DT_w \qquad (2.6)$$

where A, B, C, and D are empirical constants valid in the certain wall temperature and vapor pressure ranges. Examples of the above constants for 1 μm and 10 μm pore diameters and q''_{pore} expressed in W/cm^2 are presented in Table 2.1

Pore diameter, μm	1	10
Temperature range,	95-100	95-100
Pressure range, kPa	50-100	50-100
A	$7.0842*10^1$	$-6.9897*10^1$
B	$1.0191*10^{-3}$	$5.5748*10^{-3}$
C	$4.6829*10^{-8}$	$2.5658*10^{-4}$
D	$4.8286*10^1$	-9.1447

Table 2.1. Empirical fit parameters

Evaporation model has been developed for a single pore. Back side boiling phenomena evaluation model has been developed on its basis.

CHAPTER SUMMARY

The pore evaporation rate, calculated from a first principles evaporation model developed by Oinuma[2], is a function of many parameters, nevertheless analysis showed that it can be well represented as a function of wall temperature and vapor pressure for engineering calculations. Simplified model is used in the following chapters for evaporator geometry optimization

CHAPTER III

ANALYTICAL CALCULATION

INTRODUCTION

This chapter describes proposed concept design, manufacturing and operating limitations which must be satisfied, and design difficulties which were discovered. The iteration process described in this chapter includes the application of the FPEM model for loop heat pipe design never before applied to heat pipe technology. A design concept has been found to satisfy all limitations and goals.

IMPORTANT OPERATING LIMITATIONS

Conventional heat pipe design is based on geometry parameter variation to satisfy a number of limitations for a known working fluid. Such limitations include capillary, viscous, sonic etc. Calculations are usually performed for bulk working fluid parameters. In this work more detailed evaporator calculation has been done.

A coherent pore wick structure is shown in Figure 3.1. The vapor channel, shown in Figure 3.2, has right triangle cross-section due to photolithographic limitations. The evaporator structure can be divided into a number of identical unit cells with width W

and length L. Single cell calculations allow taking into account such effects as temperature distribution in the wick and the resulting non uniform evaporation rate.
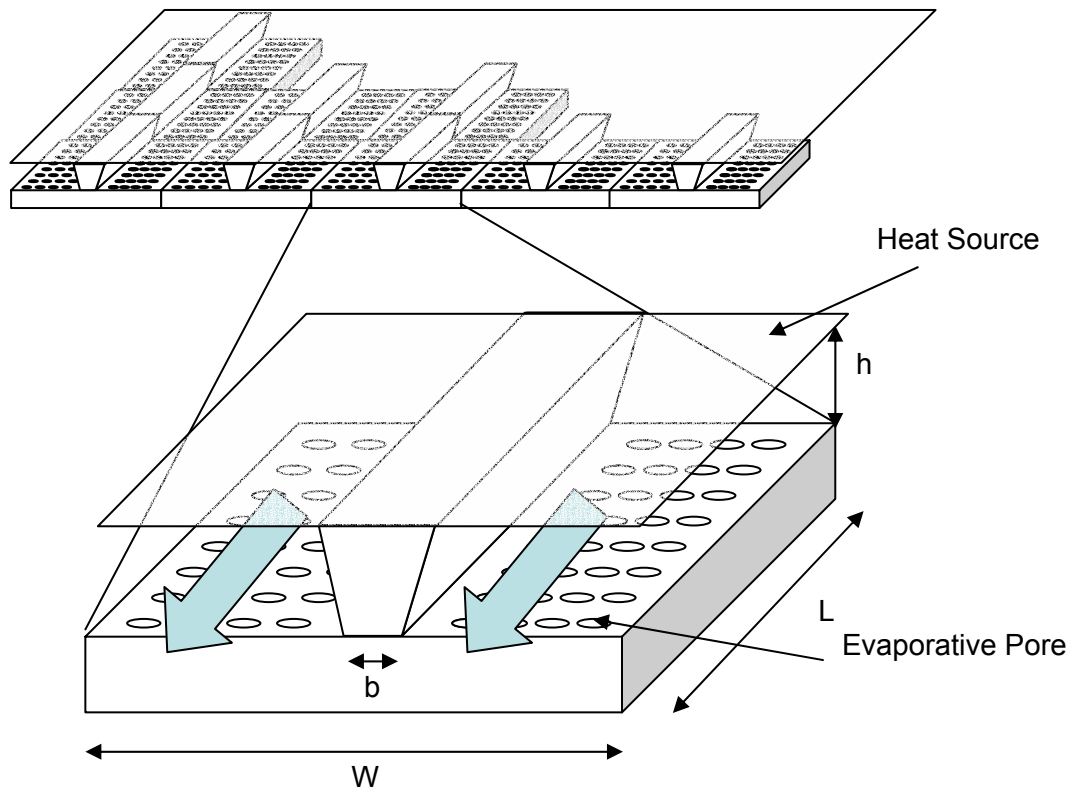
Figure 3.1. Evaporator structure

Three unit cells are shown in Figure 3.3. L is total heat source length, h is post height, t is pore length, b is post bottom width. The heat source is square; therefore the sum of all W equals L. Another manufacturer limitation is wall thickness. Neither t nor h can exceed 200 μm, the standard thickness of a silicon wafer.
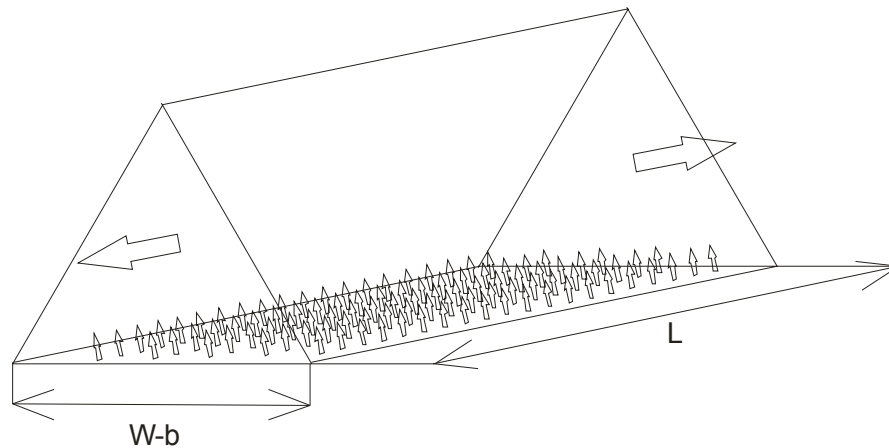
Figure 3.2. Vapor channel flow scheme

Heat pipe design starts by constructing an operating cycle plot. A typical loop heat pipe (see Figure 1.3) operating cycle (Ernst et al.[4], Richter and Gottschlich[5]) is shown in Figure 3.4. Point 1 represents the vapor state of the working fluid just above an evaporating meniscus. Point 2 represents the bulk vapor condition in the vapor path outlet. Pressure at this point is lower than point 1 due to pressure drop; however temperature is somewhat higher since the vapor receives energy from the walls. Point 3 represents the vapor transport line outlet. Here we assume adiabatic transport line walls. Point 4 represents the liquid state at the condenser outlet. Point 5 represents the liquid at the transport line outlet. Point 6 represents the superheated liquid state at the liquid side of the evaporating meniscus. Point 6 could appear somewhat confusing; it is necessary to mention that superheated water state is metastable and can not be well represented on a P-T diagram.
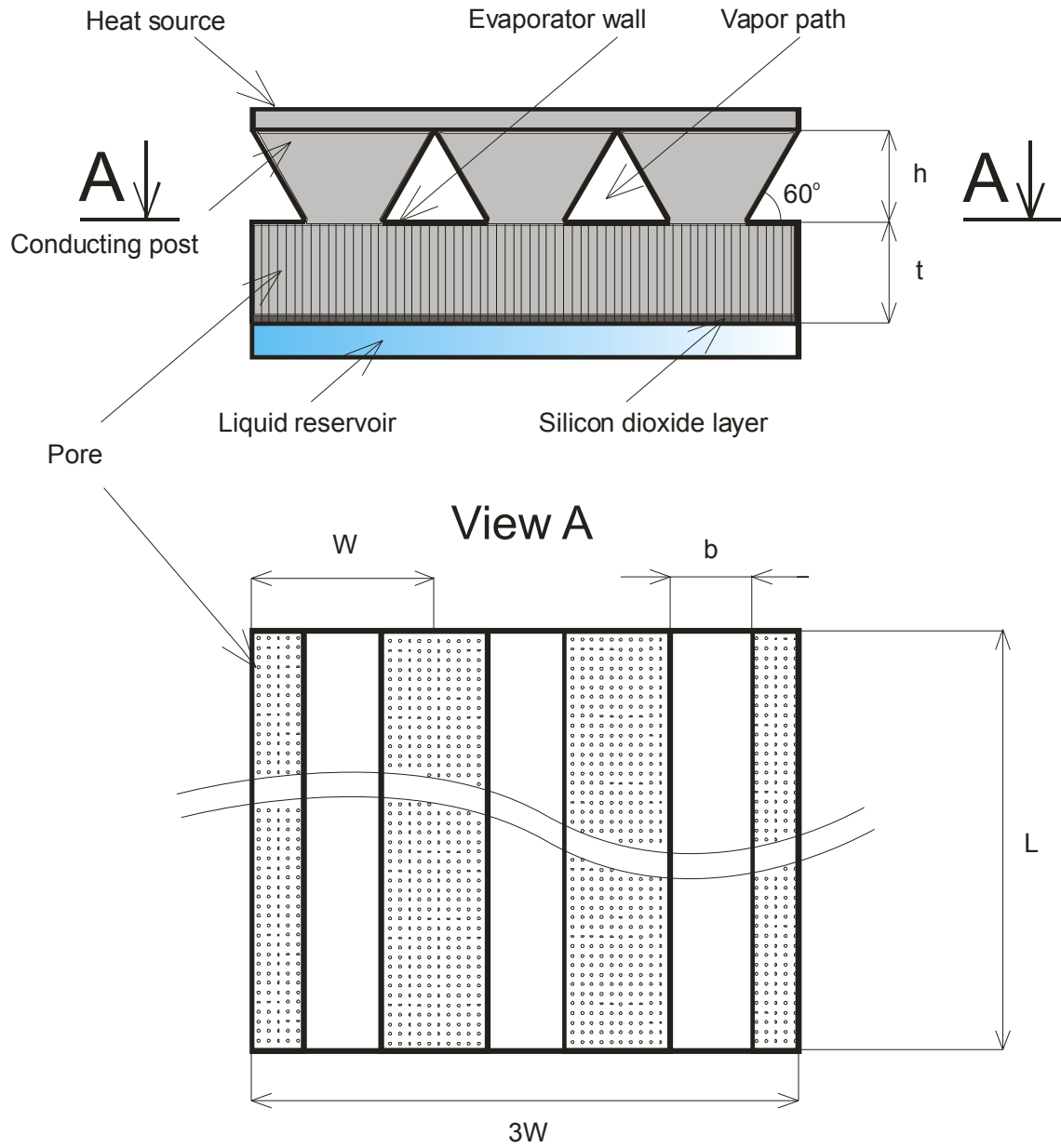
Figure 3.3. Three evaporator units
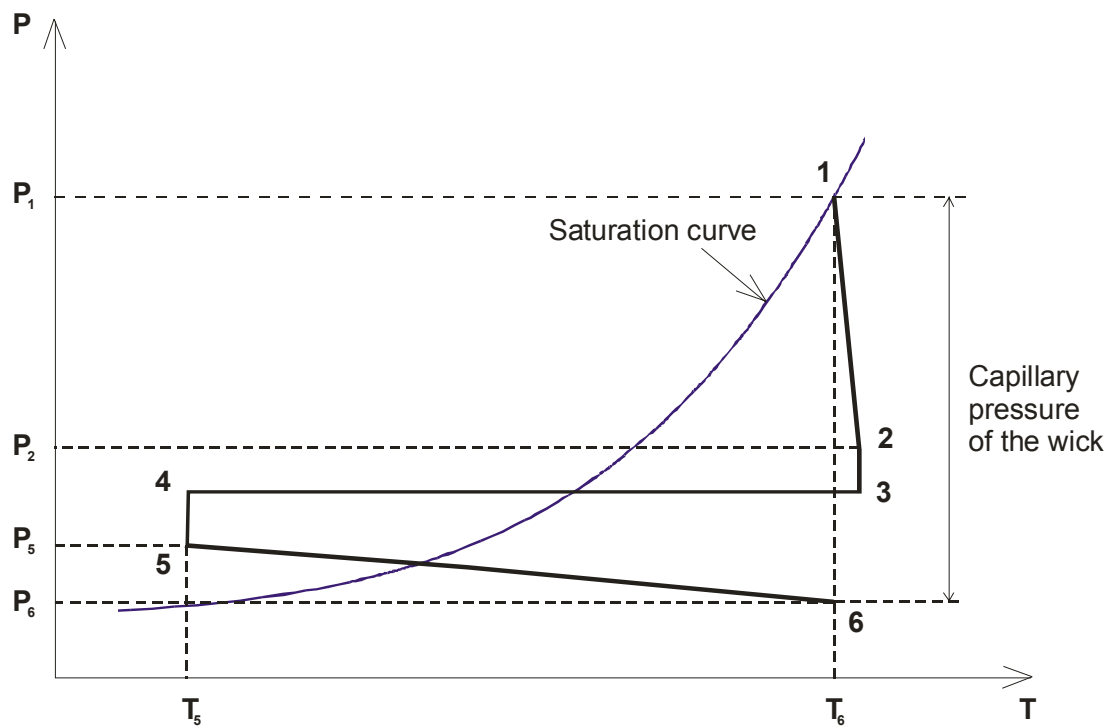
Figure 3.4. Operating cycle of a loop heat pipe

Processes 3-4 and 6-1 on the diagram correspond to phase changes – condensation and evaporation respectively. During these processes almost all heat transfer occurs at the saturation line.

Assumptions have been made to simplify calculations. The temperature at point 1 is assumed to be equal to that at point 6 and point 2. Basically this means that the temperature rise in the vapor path is assumed to be negligible. The pressure at point 6 is assumed to be equal to the saturation pressure at the condenser temperature (T5). The main points in the diagram are point 1 – which is defined by the maximally allowed temperature and saturation pressure; point 5, which is defined by lowest temperature and

pressure, higher than saturation pressure; point 6, defined by the maximal pressure drop experienced by the working fluid.

Physical processes involved in heat pipe operation limit heat pipe operational parameters. Below these limitations associated with any heat pipe design, however, their importance varies. One can see the heat pipe capillary pumping limitation from the operating cycle diagram. The capillary pressure rise of the wick must be higher than the sum of all pressure drops experienced by the working fluid in going through a process cycle. For the proposed design, the balance is given by Equation 3.1

$$\Delta P_c \geq (\Delta P_v + \Delta P_l)_{\text{transport lines}} + (\Delta P_v)_{\text{vapor channel}} + (\Delta P_l)_{\text{pore}} \qquad (3.1)$$

where ΔP_c is capillary pressure head, ΔP_v is vapor pressure drop, ΔP_l is liquid pressure drop in the transport line, vapor channel and pore. The maximum capillary pressure rise can be calculated using the La Place equation for a stationary interface, obtained from an interface force balance (Carey[8]) Equation 3.2

$$\Delta P_c = \frac{2\sigma \cos \vartheta}{R_c} \qquad (3.2)$$

where σ is the surface tension, θ is the contact angle, R_c is the radius of curvature (equal to pore radius if the pore shape is a circular cylinder).

There is an uncertainty associated with the contact angle value. No reliable data for the silicon-water interface at the pore diameter range of interest has been found. Therefore preliminary calculations were performed assuming $\cos\theta$ is equal to unity. This uncertainty is taken into account in the final design.

The friction pressure drop dominants both vapor and liquid pressure drops and other pressure losses (acceleration, gravity, form) can be neglected. Therefore Equation 3.3 is used to calculate the pressure drop.

$$\Delta P_f = f \frac{L}{d} \frac{\rho V^2}{2} \tag{3.3}$$

where ΔP_f is working fluid (liquid or vapor) friction pressure drop, f is Darcy friction factor, L is path (transport line, vapor channel, pore) length, d is path hydraulic diameter, ρ is working fluid density, V is working fluid velocity. It has been found that the turbulent flow regime never occurs in any path. Therefore f has been calculated as

$$f = \frac{64}{Re} \tag{3.4}$$

where Re is Reynolds number

$$Re = \frac{\rho V d}{\mu} \tag{3.5}$$

where μ is working fluid absolute viscosity.

Using the above definitions the pressure drop in the vapor transport line is calculated as

$$\left(\Delta P_V\right)_{transport\ line} = \left(\ f\frac{L}{d}\frac{\rho V^2}{2}\ \right)_{transport\ line} \tag{3.6}$$

Vapor transport line length has been chosen arbitrarily as 0.5 m, diameter $5.0*10^{-3}$ m has been chosen to minimize associated pressure drop. Velocity can be calculated from the mass flow rate. The mass flow rate calculation is based on the assumption that all energy transferred to the chip goes into the evaporation process as seen in Equation 3.7.

$$q''_{chip}\ L^2 = \dot{m}_{total}h_{fg} \tag{3.7}$$

$$V_V^{tr\ line} = \frac{\dot{m}_{total}}{A_{tr\ line}\rho_V} \tag{3.8}$$

where $A_{tr\ line}$ is the transport line cross sectional area. The Reynolds number

$$Re_V^{tr\ line} = \frac{\rho_V V_V^{tr\ line} d_{tr\ line}}{\mu_V} \tag{3.9}$$

where μ_v is vapor absolute viscosity.

Liquid transport line, liquid pore and vapor channel pressure drops calculations are identical in form to the above calculation. It should be mentioned that mass flow rate has to be calculated per one pore for liquid pressure drop in the pore. Hydraulic diameter and friction factor have been calculated using White's[9] recommendation for a triangular vapor channel pressure drop

$$d_V^{channel} = \frac{2h}{3} \qquad (3.10)$$

where h – triangle height (equal to post height),

$$f = 4C_f = \frac{13.333}{Re_V^{channel}} \qquad (3.11)$$

where C_f is Fanning friction factor.

Another pressure limitation is associated with the maximal pressure difference in the system from a thermodynamic point of view. Later this limitation will be called the thermodynamic pressure limit. The lowest system pressure is at point 6, where it is assumed to be equal to the saturated pressure for condenser (ambient) temperature. Here it should be mentioned that actual internal condenser temperature is higher than ambient temperature, in the same way as internal evaporator temperature is lower than chip

surface temperature due to the wall temperature gradient. Nevertheless as mentioned, the temperature gradient is expected to be small and therefore is not applied for design calculation simplicity.

The highest system pressure is at point 1, which corresponds to saturation pressure at temperature T_6. The temperature at point 6 can be found knowing the temperature gradient at the post and the chip surface temperature distribution. The temperature gradient at the post has been calculated using a 1D conduction model shown in Figure 3.5.
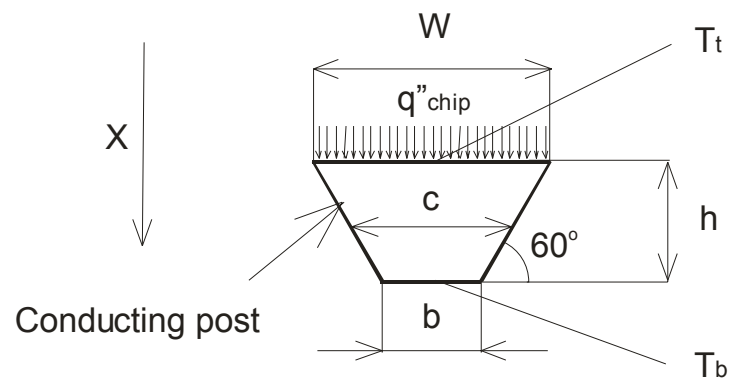
Figure 3.5. One dimensional heat conduction post model

Performing an energy balance for the post and assuming steady state conditions with negligible side heat losses

$$\dot{E}_{in} - \dot{E}_{out} = 0 \tag{3.12}$$

it follows that

$$\dot{E}_{in} = \dot{E}_{out} = q_x \tag{3.13}$$

$$q_x = q''_{chip} LW \tag{3.14}$$

and that q_x is constant with position x. Even thought the temperature distribution is a function of x and y, a one-dimensional distribution can be assumed here since side energy losses are expected to be negligible and all energy is expected to be transferred in the x direction. Conduction analysis is performed using Fourier's law. The rate equation can be integrated even without knowing the temperature distribution, since the conduction rate q_x is constant. Assuming constant post conductivity k

$$q'' = -k \frac{dT}{dx} \tag{3.15}$$

$$q_x \int_0^h \frac{dx}{A(x)} = -\int_{T_t}^{T_b} k dT \tag{3.16}$$

Cross sectional area can be expressed as

$$A(x) = c(x)L \tag{3.17}$$

where $c(x)$ is the post thickness, a linear function of x. The linear function can be found, knowing two points.

$$c(0) = W; \; c(h) = b \tag{3.18}$$

$$c(x) = \frac{x(b - W) + hW}{h} \tag{3.19}$$

Substitute $A(x)$ into Equation 3.16

$$q_x \int_0^h \frac{hdx}{(x(b - W) + hW)L} = -\int_{T_t}^{T_b} kdT \tag{3.20}$$

after simplification

$$q_x \frac{h}{L} \int_0^h \frac{dx}{x(b - W) + hW} = -\int_{T_t}^{T_b} kdT \tag{3.21}$$

after integration

$$q_x \frac{h}{L} \frac{1}{(b-W)} \ln(x(b-W)+hW)\big|_0^h = -kT\big|_{T_t}^{T_b} \tag{3.22}$$

substitute limits

$$q_x \frac{h}{L} \frac{1}{(b-W)} \big(\ln(hb-hW+hW-\ln(hW)\big) = -k(T_b-T_t) \tag{3.23}$$

after simplification

$$q'' LW \frac{h}{L} \frac{1}{(b-W)} \ln\left(\frac{hb}{hW}\right) = k(T_t-T_b) \tag{3.24}$$

Finally

$$\Delta T_{post} = \frac{q''_{chip} \, Wh \ln\left(\dfrac{b}{W}\right)}{k(b-W)} \tag{3.25}$$

where ΔT_{post}

$$\Delta T_{post} = T_t - T_b \tag{3.26}$$

is the temperature difference between top and bottom of the conducting post.

Liquid entrainment from the wick in the vapor stream due to high liquid vapor shear forces is another limitation. The viscous limit, based on vapor phase friction, limits working fluid circulation. The sonic limit occurs when vapor flow achieves the speed of sound, usually at the condensation zone of a liquid metal heat pipe. For the present design, liquid entrainment, viscous limit and sonic limit are not important.

ITERATION CALCULATIONS

Vapor channel geometry has been varied for the first iteration calculation. It has been optimized to achieve a total pressure drop value lower or equal to the capillary pressure available and the thermodynamic pressure limit. The vapor channel cross section is a right triangle, therefore its size can be described by either side length or height. Triangle height has been adjusted to achieve the smallest value which satisfies pressure limitations.

The first iteration calculations have been performed for different pore diameters; however pore number on the channel width was constant (Figure 3.6).

Pores at the center of the evaporator between posts have smaller evaporation rates than at the posts due to the evaporator temperature drop as it is qualitatively shown in Figure 3.7. Therefore there is an optimal pore and post spacing. Calculation of the above phenomena is complicated by the wick geometry and temperature dependent

evaporation rate. The numerical model developed to carry out this optimization is described in the following chapter.
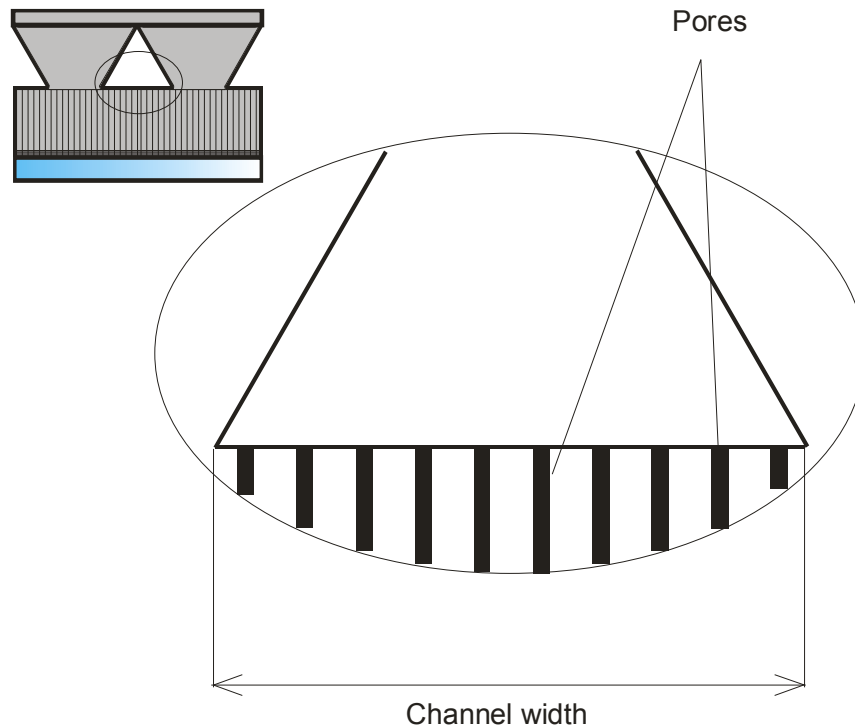
Figure 3.6. Pores on the vapor channel width

For sample calculation purposes, it was decided to have 10 pores on the channel width, since the number of the pores was not defined at the initial calculation stage. Total pore number was calculated using a square lattice assumption.

The calculation was carried out as follows. First iteration geometry parameters are presented in Table 3.1. The resulting pressure drop values are presented in Table 3.2.
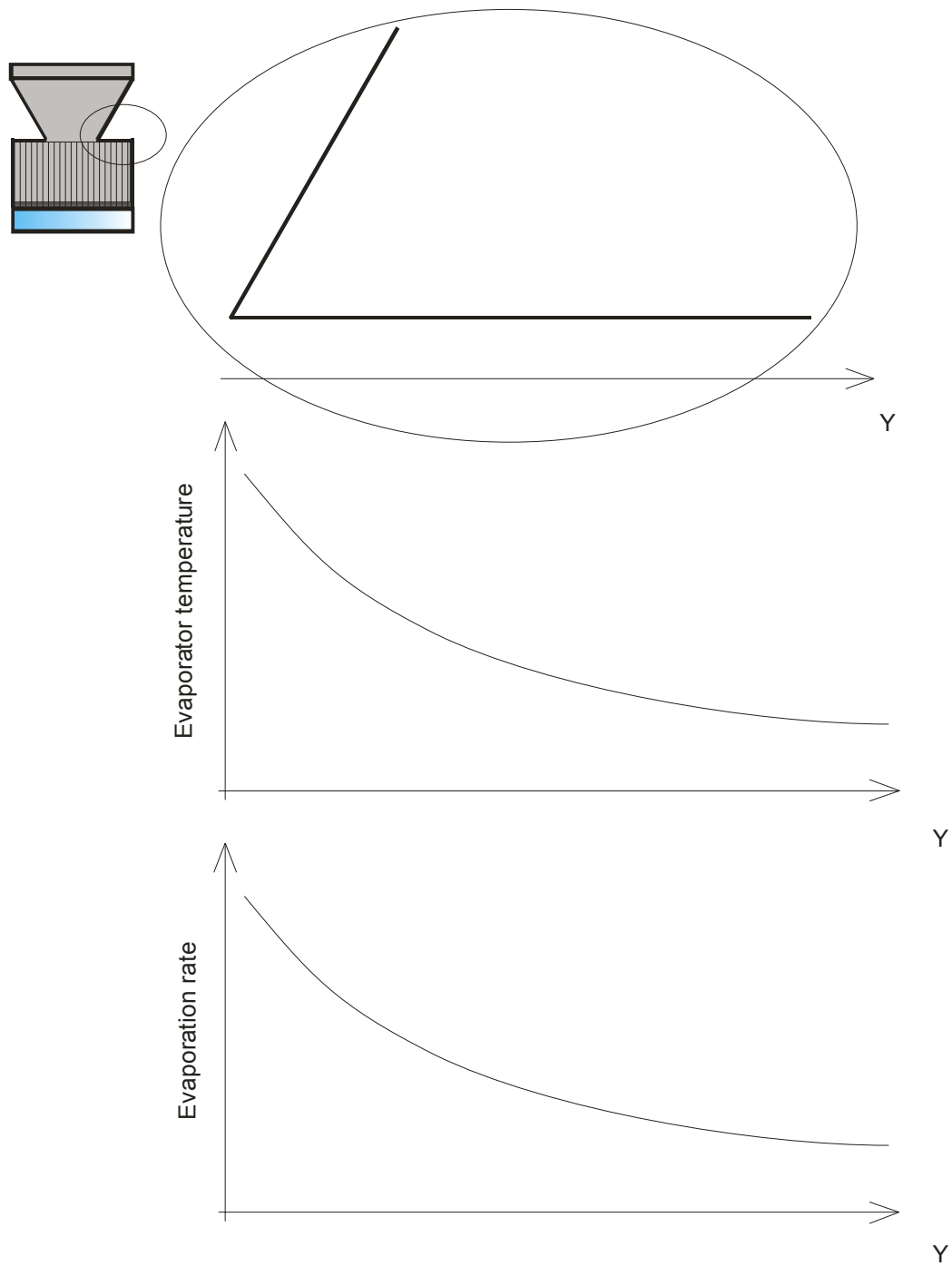
Figure 3.7. Qualitative evaporator temperature and resulting evaporation rate distributions

Parameters	Geometry 1	Geometry 2	Geometry 3
Pore diameter, μm	10	5	2
h, μm	135	108	88.5
t , μm	200	200	200
b, μm	10	10	10
Pitch/d ratio	1.559	2.494	5.110
Pore # on the width	10	10	10
Total pore#	6410	8010	9780

Table 3.1. First calculation iteration geometry parameters

Pressure drop		Value, Pa		
Working fluid	Component	Geometry1	Geometry2	Geometry3
Vapor	Transport line	29.09	29.09	29.09
Liquid	Transport line	0.43	0.43	0.43
Liquid	Pore	27.54	286.39	7631.00
Vapor	Vapor channel	23163.89	45923.80	84825.32
Total		23220.96	46239.72	92485.85
Capillary limit		23552.00	47104.00	111760.00
Thermodynamic pressure limit		88823.10	91228.38	92891.05

Table 3.2. First calculation iteration pressure drop values

One can see that for 10 μm and 5 μm pore diameters, the capillary limit is lower than the thermodynamic limit, whereas for 2 μm and lower pore diameters the thermodynamic limit is dominant. Further, each geometry satisfies the required versus available pressure drops.

Liquid pressure drop in the pore rises with decreasing pore diameter and for a 1 μm pore diameter exceeds the thermodynamic limit. A minimum pore diameter of 1.5

μm has been found to satisfy the thermodynamic limit. This occurs due to the pore number assumption.

Hydraulic calculations have been performed on the basis of energy conservation. All energy transferred to the chip is assumed to be utilized by the evaporation process. A simple energy balance can be applied for an evaporator unit cell

$$q''_{pore} A_{evap} = q''_{chip} LW \qquad (3.27)$$

where evaporation surface A_{evap}

$$A_{evap} = N_{pore} A_{pore} \qquad (3.28)$$

and N_{pore} is the number of the pores in one unit cell of dimensions LW. Here it should be noted that q''_{pore} found from Equation 3.27 represents the minimal heat flux value which must be achieved by the pore to balance inlet thermal energy. The real heat flux achieved by the pore is a function of pore wall temperature, vapor pressure and pore diameter as shown in Chapter II and can be different from q''_{pore}. To avoid misunderstanding, the real heat flux achieved by the pore is called either real heat flux or FPEM evaporation rate expressed in terms of heat flux. Heat flux found from Equation 3.27 is called the energy balance heat flux. Performed calculations showed that operating temperature increasing, in case when balance heat flux exceeds real heat flux,

does not lead to higher evaporation rate since saturation pressure also increases (see Figure 2.7). Operating temperature decreasing in case when real heat flux exceeds balance heat flux does not lead to lower evaporation rate. Design limitations are met when the real heat flux is equal to energy balance heat flux. This requirement called the energy balance limitation later in the text. FPEM heat flux is different for each pore due to evaporator temperature difference (see Figure 3.7). Therefore real heat flux value, compared to balance heat flux, should be calculated as average of all pore heat flux values. This effect was taken into account in optimal model design, described in Chapter V.

Thermodynamic cycles for the above results are shown in Figures 3.8 – 3.10.
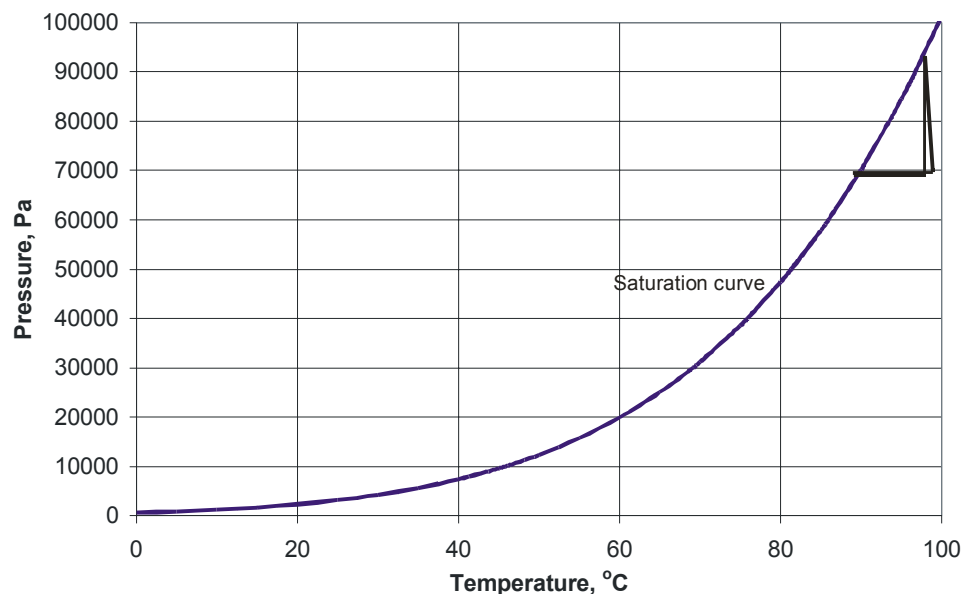
Figure 3.8. Loop heat pipe cycle for 1st geometry
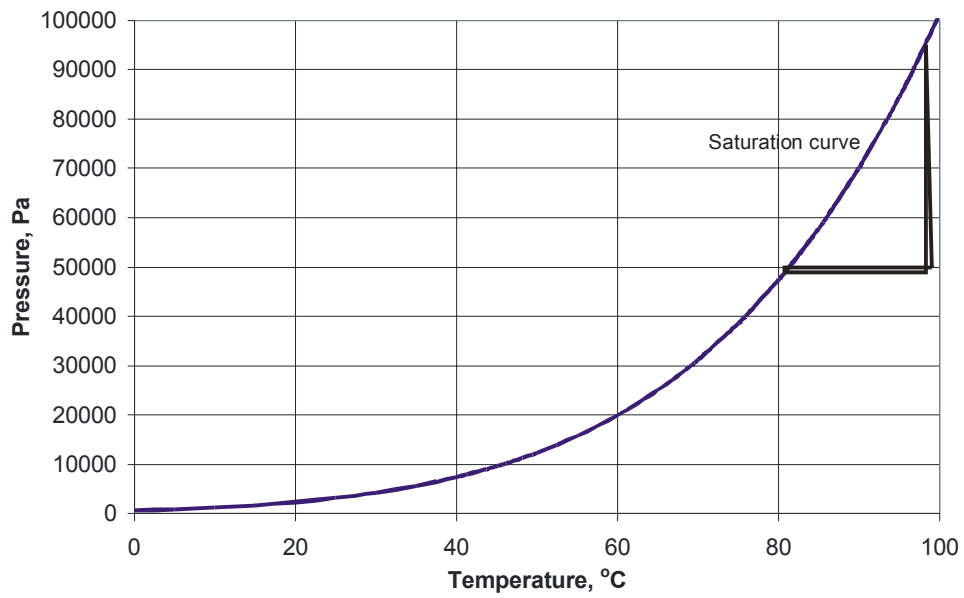
Figure 3.9. Loop heat pipe cycle for 2nd geometry
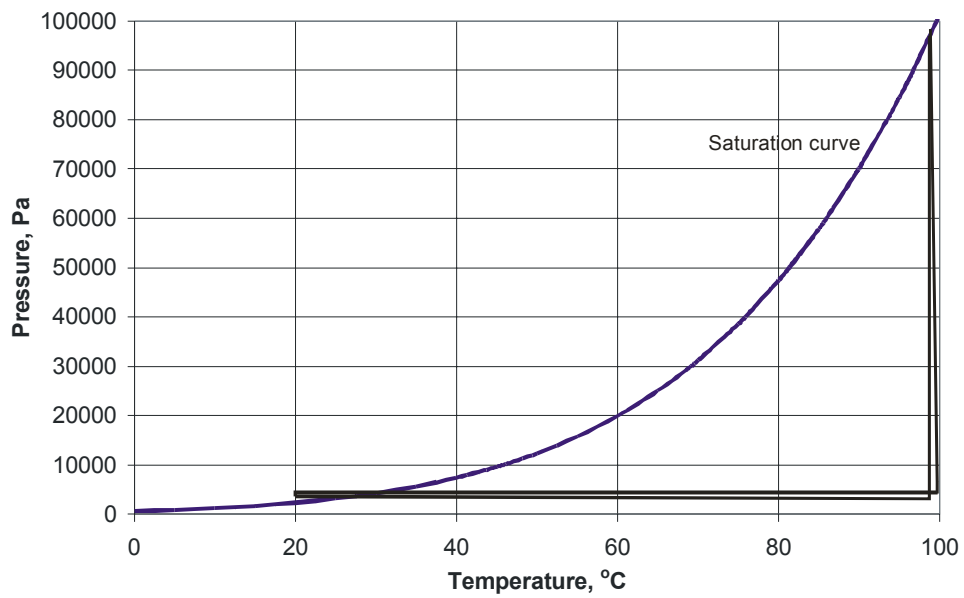
Figure 3.10. Loop heat pipe cycle for 3rd geometry

The thermodynamic cycle defines the minimal condenser temperature which is different for all geometries as can be seen. It has been assumed that 10^oC is maximal allowed temperature difference (see Chapter II). The third geometry is inappropriate based on this statement, i.e. the LHP ΔT is too large for practical applications.

Vapor pressure varies between the center of the vapor channel and its periphery due to vapor pressure drop. The evaporation rate, calculated on the basis of the first principles evaporation model, is highly dependent on vapor pressure as has been shown in Chapter II. Therefore the evaporation rate differs significantly along the vapor channel length.

The evaporation rate can be approximated as a linear function of vapor pressure for a given liquid temperature in the range of interest. This allows using average vapor pressure in the vapor channel to find the average evaporation rate. Each geometry evaporation rate was found knowing the average vapor channel pressure, pore diameter and pore wall temperature which is approximated using Equation 3.29. Then the evaporation rate is expressed in terms of heat flux and compared with the energy balance heat flux.

$$T_w = T_{chip} - \Delta T_{post} \qquad (3.29)$$

Figure 3.11 represents both heat fluxes for all above geometries. Two curves do not cross; therefore none of the above geometries satisfy design goals.
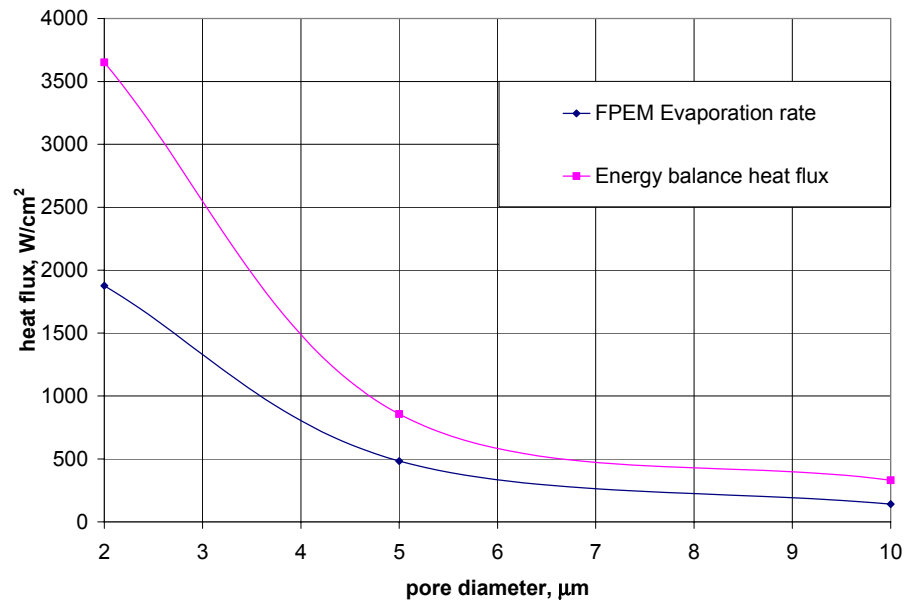
Figure 3.11. First calculation iteration heat fluxes comparison

One of the ways to achieve the required balance is to increase the total pore number for the same post-to-post spacing. A second iteration of calculations was performed for a pitch to diameter ratio of 1.5. Geometry parameters are presented in Table 3.3.

Parameters	Geometry 1	Geometry 2	Geometry 3
Pore diameter, μm	10	5	2
h, μm	135	108	88.5
t, μm	200	200	200
b, μm	10	10	10
Pitch/d ratio	1.5	1.5	1.5
Pore # on the width	10	16	34
Total pore#	6660	21312	113288

Table 3.3. Second calculation iteration geometry parameters

Pressure drop values are presented in Table 3.4.

Pressure drop		Value, Pa		
Working fluid	Place	Geometry1	Geometry2	Geometry3
Vapor	Transport line	29.09	29.09	29.09
Liquid	Transport line	0.43	0.43	0.43
Liquid	Pore	26.51	107.64	658.77
Vapor	Vapor channel	23163.89	45923.80	84825.33
Total		23219.92	46060.96	85513.61
Capillary limit		23552.00	47104.00	111760.00
Thermodynamic pressure limit		88823.10	91228.38	92891.05

Table 3.4. Second calculation iteration pressure drop values

Thermodynamic cycles for calculated geometries can be assumed the same as for first calculation iteration, since main geometry parameters are identical and pore pressure drop change is insignificant compared with overall pressure drop. Nevertheless the liquid pressure drop change due to increased pore number would allow lowering the 1.5 µm pore diameter to satisfy the thermodynamic pressure limit. Heat fluxes for the second iteration are presented in Figure 3.12.

One can see that the energy balance heat flux curve does not depend on pore diameter which is different compared with Figure 3.11. This can be explained by different pitch to diameter ratio for all geometries, presented in Table 3.1. Same pitch to diameter ratio used for second calculation iteration leads to equal ratio of the unit cell evaporation area A_{evap} (see Equation 3.27) to energy input area (equal to LW for one unit cell). And thus the same energy balance heat flux.

A small effect is caused by the pore number calculation scheme – the evaporation rate is counted only for full pores on the vapor channel length as shown in Figure 3.13. Thus for bigger diameter pores the evaporation rate can be slightly underestimated whereas the balance heat flux is slightly overestimated. This gives a conservative margin. Above effect can be found in Figure 3.12, where the energy balance heat flux is equal for 5 and 10 μm pores and smaller for 2 μm pore.
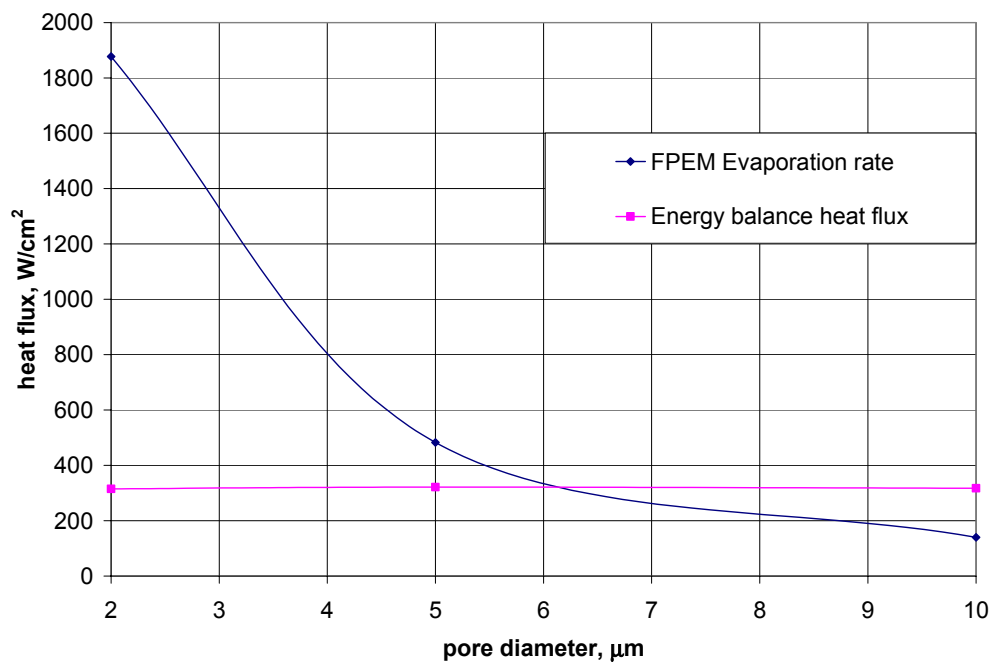
Figure 3.12. Second calculation iteration heat fluxes comparison

The geometry with a pore diameter of 10 μm has lower evaporation rate than that required to balance 100 W/cm^2 chip heat flux; whereas the geometry with a pore

diameter of 2 μm has a significantly higher evaporation rate. Figure 3.12 shows that the

energy balance limitation is satisfied for pore diameter of 6.3 μm.
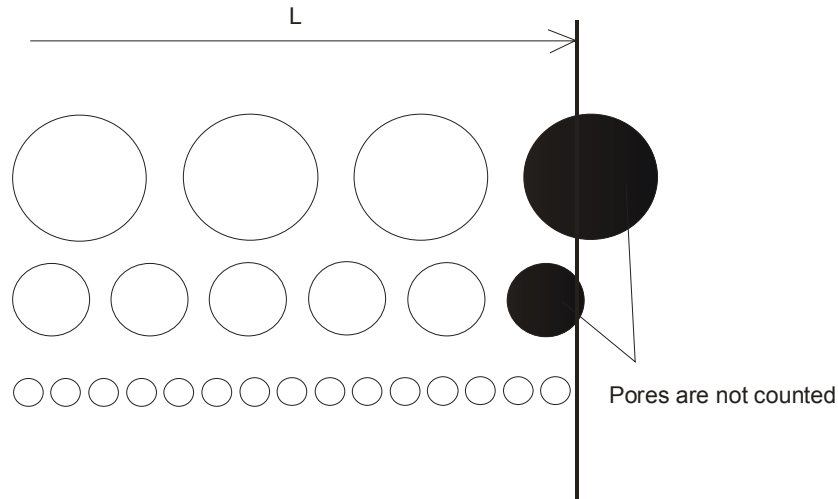
Figure 3.13. Pore counting scheme on channel length

Estimated liquid speed in the pore is about $1.5*10^{-3}$ m/sec for second calculation

iteration geometries. Pore height is 200 μm. Therefore the estimated time of water flow

through the pore is about 0.13 second. The required liquid temperature change in the

pore varies from 20 K for 10 μm pore to 80 K for 2 μm pore. A simplified conduction

model for an infinite cylinder has been applied to estimate the time necessary to change

liquid temperature from inlet to evaporation.

For an infinite cylinder of radius R, initially at the uniform temperature T_i, the

temperature distribution over a convective boundary condition (Incropera and De Witt

[10]) is described as

$$\theta^* = \sum_{n=1}^{\infty} C_n \exp(-\zeta_n^2 Fo) J_o(\zeta_n r^*) \tag{3.30}$$

θ^* is dimensionless temperature

$$\theta^* = \frac{T - T_w}{T_i - T_w} \tag{3.31}$$

where T_w is the wall temperature, r^* is dimensionless spatial coordinate

$$r^* = \frac{r}{R} \tag{3.32}$$

where r is the spatial coordinate. Fo is Fourier number

$$Fo = \frac{\alpha t}{R^2} \tag{3.33}$$

where t is time, α is thermal diffusivity.

$$\alpha = \frac{k}{\rho C_p} \tag{3.34}$$

where k is conductivity, ρ is density, C_p is heat capacity at constant pressure. J_o is zero order Bessel function.

For values of Fourier number greater 0.2, the infinite series solution can be approximated by the first term of the series

$$\theta^* = C_1 \exp(-\zeta_1^2 Fo) J_o(\zeta_1 r^*) \tag{3.35}$$

The dimensionless form of the fluid centerline temperature distribution is

$$\theta_o^* = C_1 \exp(-\zeta_1^2 Fo) \tag{3.36}$$

where θ_o^* is dimensionless centerline temperature

$$\theta_o^* = \frac{T_{cl} - T_\infty}{T_i - T_\infty} \tag{3.37}$$

T_{cl} is centerline temperature.

The Biot number

$$Bi = \frac{hR}{k} \tag{3.38}$$

where h is heat transfer coefficient, and k is water conductivity. The heat transfer coefficient equal to infinity corresponds to a constant temperature boundary condition. C_n and ζ_n are tabulated coefficients for a range of Biot numbers (Incropera and De Witt [10]). Centerline temperature as a function of time has been obtained by solving the above equations. Results are presented in Table 3.5 and Figure 3.14.

Constant	Fo	t, sec	θ	Tcl, K
	0.0996691	$1.49*10^{-5}$	0.9	364.15
	0.1200326	$1.80*10^{-5}$	0.8	365.15
Bi = ∞	0.1431188	$2.14*10^{-5}$	0.7	366.15
	0.1697699	$2.54*10^{-5}$	0.6	367.15
C_1=1.6018	0.2012915	$3.01*10^{-5}$	0.5	368.15
	0.2398708	$3.59*10^{-5}$	0.4	369.15
ζ_1=2.405	0.2896082	$4.34*10^{-5}$	0.3	370.15
	0.359709	$5.38*10^{-5}$	0.2	371.15
T_i = 363.15 K	0.4795472	$7.18*10^{-5}$	0.1	372.15
	1.275735	$1.91*10^{-4}$	0.001	373.14

Table 3.5. Infinite cylinder one-term approximation to the series solution results for transient one dimensional conduction

Note that above solution is valid for Fo > 0.2 only.

The time, necessary to change incoming liquid temperature by 10 K (10°C), obtained by using the numerical convection model described in Chapter II, is higher by about an order of magnitude. Nevertheless the time necessary to change incoming liquid temperature is orders of magnitude less than the actual time water flows through the pore, thus satisfying the sensible heating requirements.
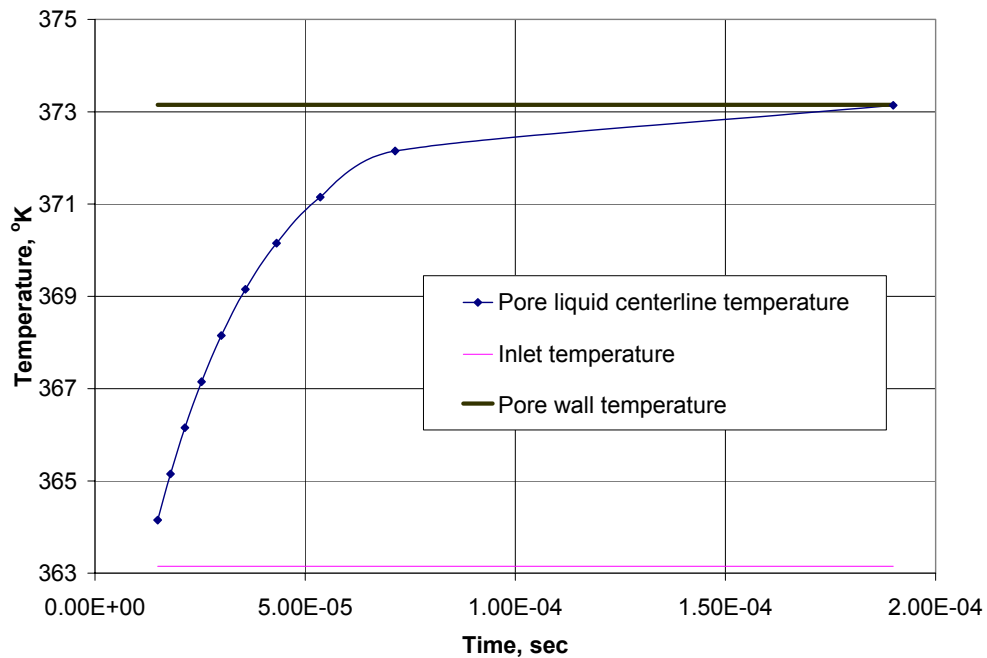
Figure 3.14. Approximate solution centerline pore temperature

A pressure level lower than atmospheric should be achieved in the condenser to satisfy design limits, as can be seen from the thermodynamic cycles (Figures 3.8-3.10). On the other hand, the maximal value for condenser pressure and condenser temperature should be sought to avoid non-condensable gases leak and to simplify heat pipe design and manufacturing. The third geometry design of Table 3.3 is inappropriate based on these limitations.

Actual capillary pressure rise (Equation 3.2) is somewhat lower than the calculated pressure rise, due to contact angle uncertainty, as mentioned. Therefore the pressure limitation (Equation 3.1) is not satisfied for first and second iteration

calculations. The total pressure drop (Tables 3.2 and 3.4) can be lowered by increasing vapor channel cross-sectional area.

The third iteration of design calculations has been performed for a vapor channel height of 200 μm, equal for all geometries. Geometry parameters are presented in Table 3.6. Pressure drop values are presented in Table 3.7. One can see that increasing vapor channel height to 200 μm considerably reduces vapor pressure drop for all geometries compared with first and second iteration calculations (Tables 3.2 and 3.4).

A negative effect of this design change is an increased post temperature drop which lowers the evaporation rate. None of the calculated geometries has a sufficient evaporation rate, as can be seen in Figure 3.15.

Pore diameter, μm	10	5	2
h, μm	200	200	200
t , μm	200	200	200
b, μm	10	10	10
Pitch/d ratio	1.5	1.5	1.5
Pore # on the width	15	30	76
Total pore#	9990	39960	253232

Table 3.6. Third calculation iteration geometry parameters

The energy balance heat flux is flat for 5 and 10 μm diameter pores and slightly different for 2 μm pore. Difference is caused by pore number counting scheme (Figure 3.13).

Pressure drop		Value, Pa		
Working fluid	Place	Geometry1	Geometry2	Geometry3
Vapor	Transport line	29.09	29.09	29.09
Liquid	Transport line	0.43	0.43	0.43
Liquid	Pore	25.67	102.68	632.93
Vapor	Vapor channel	6984.41	6984.41	6984.41
Total		7039.60	7116.61	7646.86
Capillary limit		23552.00	47104.00	111760.00
Thermodynamic pressure limit		82878.43	82878.43	82878.43

Table 3.7. Third calculation iteration pressure drop values
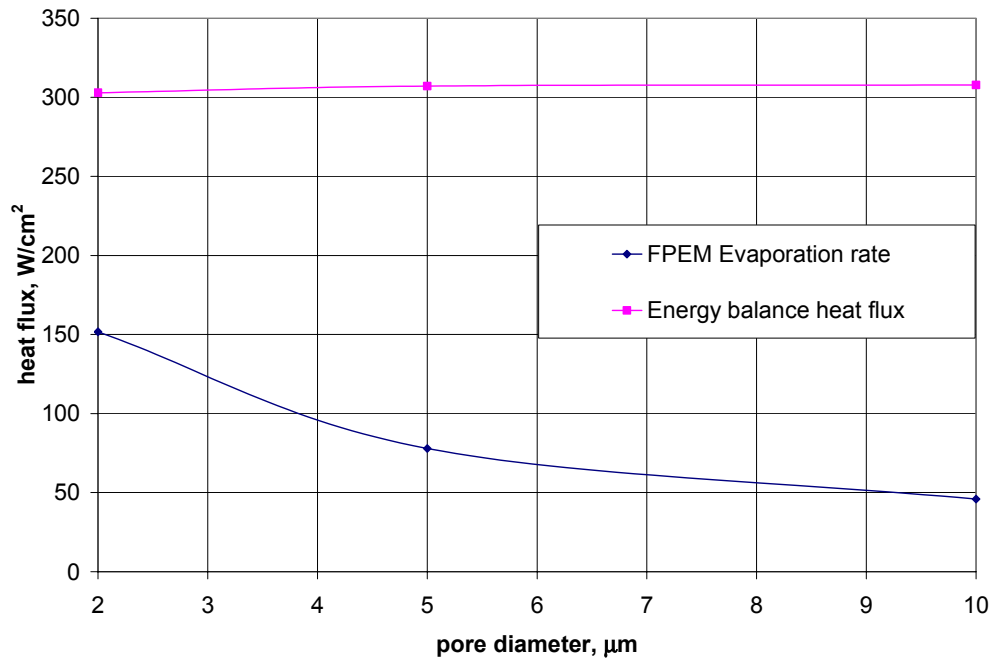
Figure 3.15. Third calculation iteration heat fluxes comparison

The pressure drop values presented in Tables 3.2, 3.4 and 3.7 show that the vapor channel pressure drop depends strongly on vapor channel geometry and that the vapor

pressure drop is higher than any other pressure drop by orders of magnitude. The transport line pressure drops are negligible compared with total pressure drop.

A general tendency can be seen from the calculations overall that lower pore diameter is more likely to achieve the required evaporation rate within operating limits. Further calculations below, using the same parameters, show that a pore diameter of 0.5 μm satisfies all limitations for pitch to diameter ratio of 1.7 and all other geometry parameters same to third iteration calculation (Tables 3.8 and 3.9). Geometry with pitch to diameter ratio of 1.5 has real heat flux exceeding energy balance heat flux. Liquid pressure drop in the pore becomes dominant for this pore diameter. Thermodynamic cycle for pitch to diameter ratio of 1.7 is shown in Figure 3.16.

Pore diameter, μm	0.5	0.5
h, μm	200	200
t , μm	200	200
b, μm	10	10
Pitch/d ratio	1.5	1.7
Pore # on the width	307	271
Total pore#	4092924	3188044
Real heat flux, W/cm^2	390.08	390.08
Energy balance heat flux, W/cm^2	299.81	384.91

Table 3.8. 0.5 μm diameter pore calculation parameters

Increased vapor channel post-to-post size can lead to a considerable conduction temperature gradient across the wick and ineffective evaporation. Accurate estimation of the above effect cannot be performed using a 1D conduction model due to the

complicated geometry and water flow in the pore. Numerical methods to solve this problem are described in the following chapter.

Pressure drop		Value, Pa	
Working fluid	Place	p/d=1.5	p/d=1.7
Vapor	Transport line	29.09	29.09
Liquid	Transport line	0.43	0.43
Liquid	Pore	10024.85	12870.26
Vapor	Vapor channel	6984.41	6984.41
Total		17038.78	19884.19
Capillary limit		471040.01	471040.01
Thermodynamic pressure limit		82891.49	82891.49

Table 3.9. 0.5 µm pore diameter calculation pressure drop values
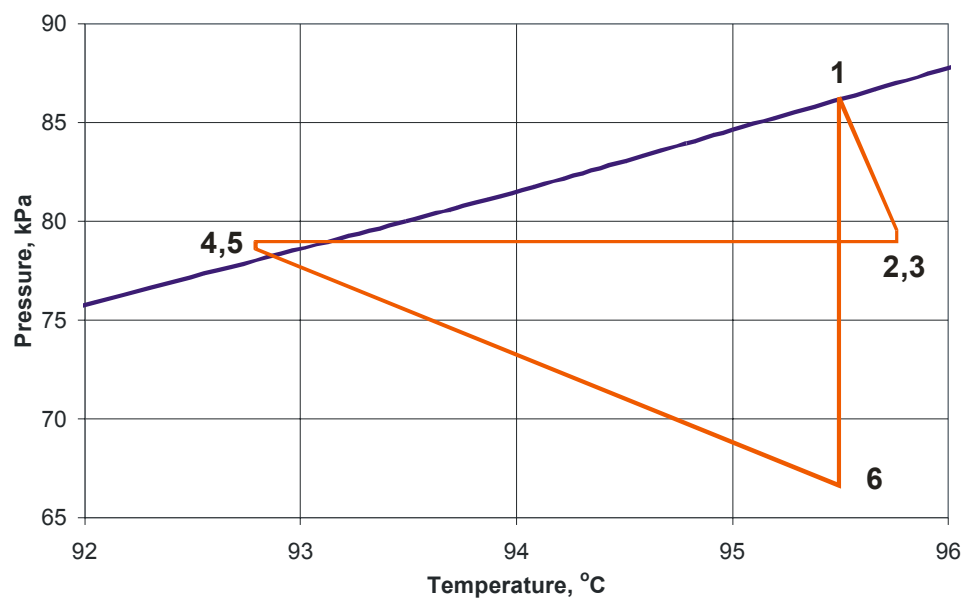
Figure 3.16. Loop heat pipe cycle for 0.5 µm pore

CHAPTER SUMMARY

An iteration process applied in this chapter gives information for the optimal design calculation. Several recommendations can be formulated on the basis of the performed calculations. Lower pore diameter is more likely to achieve required evaporation rate within operating limits. The minimum pitch to diameter ratio allowed should be used. Vapor channel cross-sectional area change significantly affects evaporation rate. Liquid pressure drop in the pore becomes the dominant pressure drop term with pore diameter decreasing and channel cross sectional area increasing.

A number of parameters defining loop heat pipe operation were found necessary to estimate LHP performance. Overall numerical performance modeling is described in the following chapter.

All calculations have been implemented in a FORTRAN program "Evaporator" listed in Appendix 2.

CHAPTER IV

NUMERICAL CALCULATION

INTRODUCTION

This chapter describes numerical models used to create post bottom width, pore number, and pitch-to-diameter ratio optimization recommendations. A number of calculations were performed to evaluate evaporation rate and backside temperature on the basis of evaporator temperature distribution.

Although none of the geometries with pore diameter of 10 μm has been found to be viable design due to energy balance limitation, numerical calculation has been performed for third calculation iteration geometry with pore diameter of 10 μm for simplicity, assuming that energy balance limitation is met. It has been found unreasonable to model geometry with tens of pores on the channel width due to used CPU time. General recommendations, obtained on the basis of this calculation can be used for any of the described in previous Chapter geometry since all processes are identical.

Numerical codes are valuable tools for evaluation of temperature distribution, pressure drop, etc. in cases when analytical methods are found either inapplicable or complicated. The Computational Fluid Dynamics (CFD) software STARCD showed a

big potential for future application in heat pipe technology when accompanied by the first principles evaporation model. Results, described in this chapter, have never been obtained before for loop heat pipe design.

NUMERICAL MODELS

Two numerical models have been developed for the evaporator design. Loop heat pipe power assumed equal to 100 W for all calculations.

The first model, schematically shown in Figure 4.1, represents a full length triangular vapor channel and post. The purpose of this model is to evaluate pressure drop and temperature distribution in the vapor path. Vapor velocity is calculated in accordance with the geometry of the evaporator.
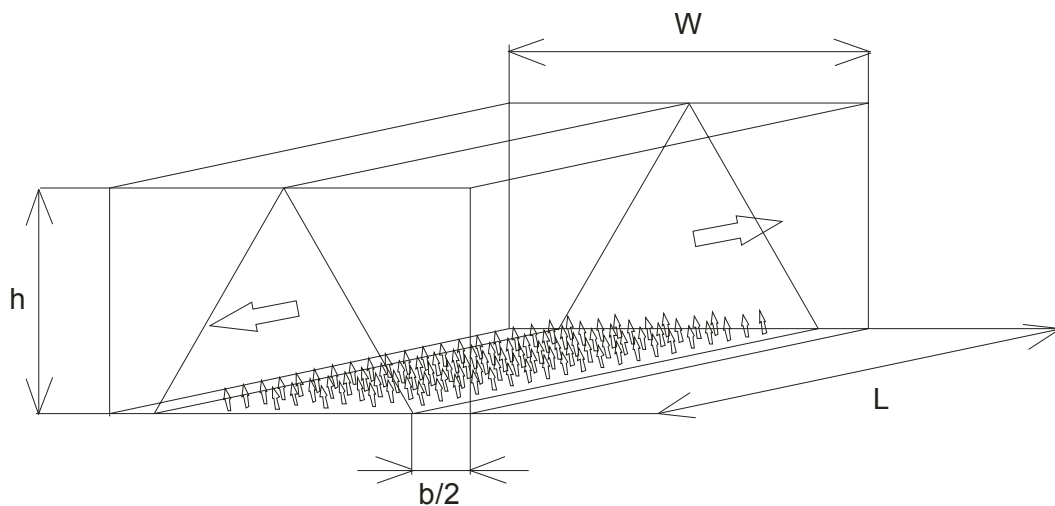
Figure 4.1. Vapor triangular channel geometry numerical model scheme

A constant temperature boundary, found from the conduction heat transfer calculation, is applied at the top and bottom of the post structure. Main geometry parameters and pressure drop, found analytically, are presented in Table 4.1. Results are shown in Figures 4.2-4.4.

Numerical calculation of vapor pressure drop is shown in Figure 4.2 as the difference between local maximal and local minimal pressure. Total pressure drop is equal 26.2 kPa. The negative value of the local minimal pressure should not be confusing since relative pressure is shown. One can see that vapor channel pressure drop, calculated using numerical model, is significantly lower than the analytical model result, presented in Table 4.1. It can be explained by numerical model calculation scheme, calculating pressure drop for square rather than triangular shape.

Parameter	Value
Channel height, μm	135
Unit cell/channel length, m	0.01
Top temperature, K	373.15
Bottom temperature, K	369.15
Analytical pressure difference, kPa	45.9

Table 4.1. First numerical model parameters

Vapor temperature rise of 0.3 K (0.3°C) was found as the difference between average vapor temperature at the channel outlet and average vapor temperature at the channel center. Temperature distributions at the channel outlet and the channel center are presented in Figures 4.3 and 4.4 accordingly. Found vapor temperature rise is

applied in thermodynamic cycle. Note that vapor temperature is higher than liquid temperature, which was set equal to the temperature under the post.
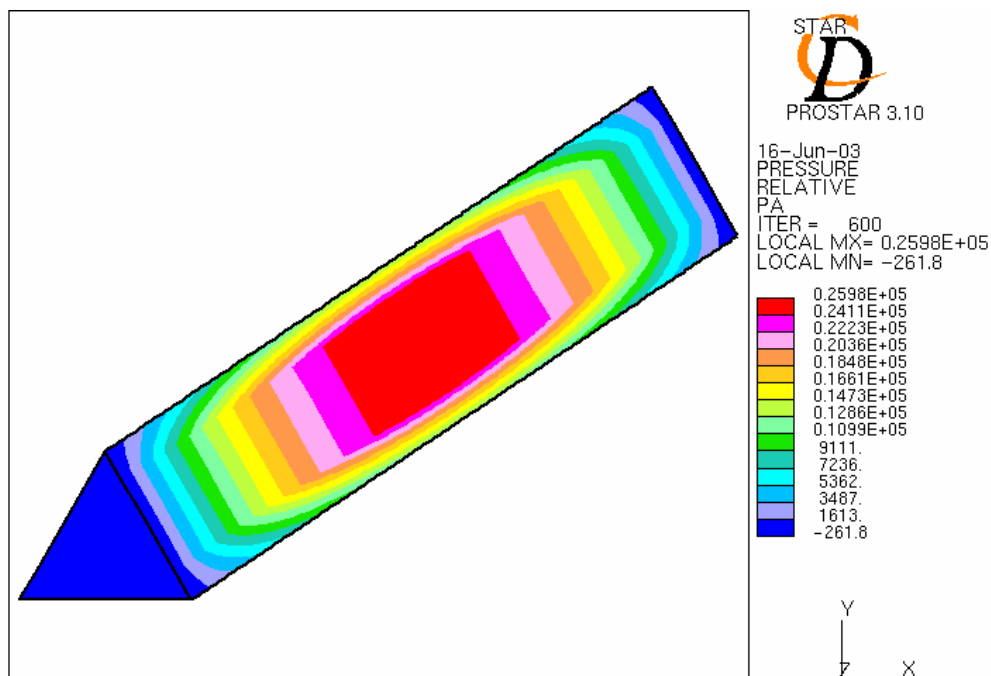
Figure 4.2. Vapor pressure drop numerical calculation

The second geometry model, which nodalization is schematically shown in Figure 4.5, represents half of the unit cell evaporator porous structure with bottom fluid reservoir. Model nodalization detailed view is shown in Figure 4.6. The model has been constructed in order to find the temperature distribution in the porous structure, pore number and post bottom width for optimum operation.
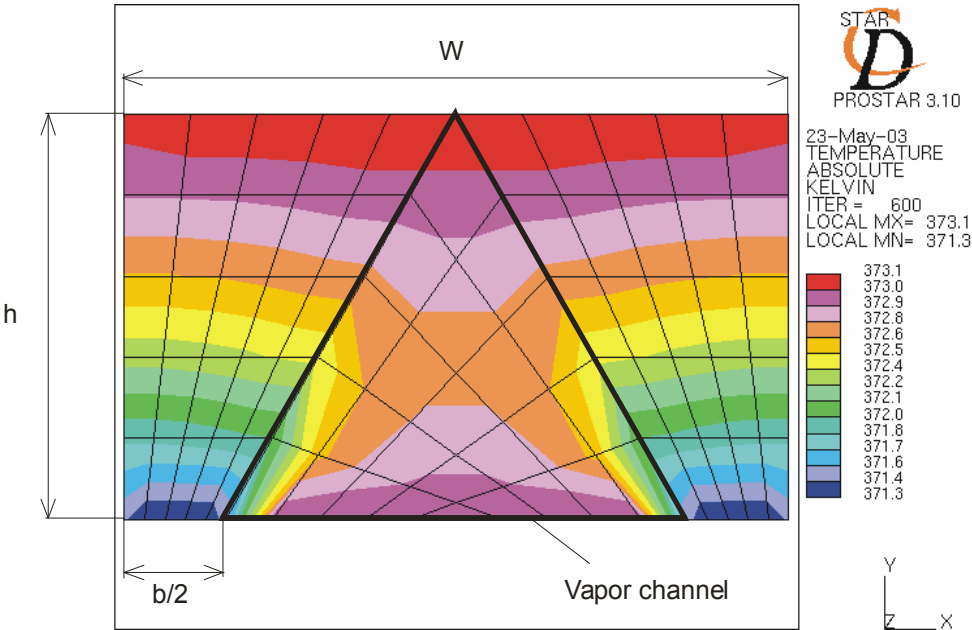
Figure 4.3. Vapor channel center cut temperature distribution
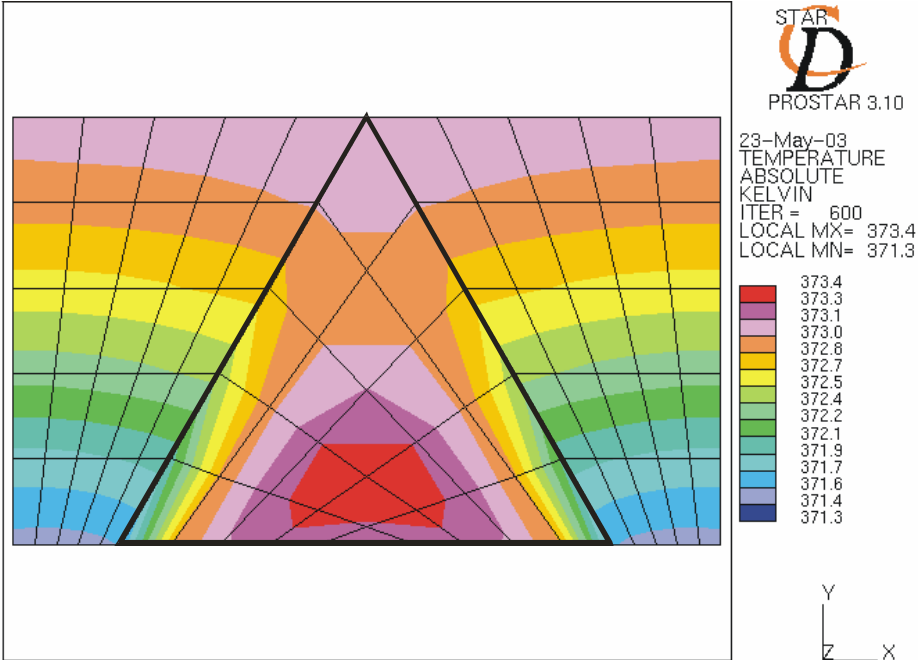
Figure 4.4. Vapor channel outlet temperature distribution
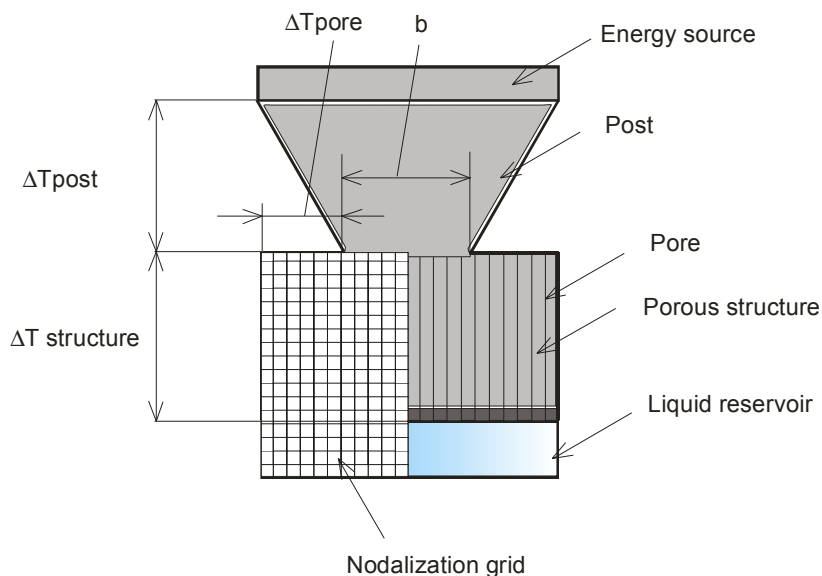
Figure 4.5. Evaporator wall numerical model

Boundary conditions were set as follows: constant heat flux boundary at the post bottom, calculated on the basis of chip heat flux (Equation 4.1) and assuming all energy transferred through the post to the evaporator; temperature dependent pore heat flux; symmetry boundary at the side walls; and adiabatic boundary at the bottom. Since each pore has a different associated wall temperature, a pore specific temperature dependent boundary, found on the basis of analytical calculation, is set for each pore (Equation 4.2), where: q''_{pore} (W/cm^2), T_w (^{o}C). Heat flux function has been found assuming that FPEM evaporation rate is equal to the energy balance heat flux. This was achieved by applying lower vapor pressure, than found analytically.
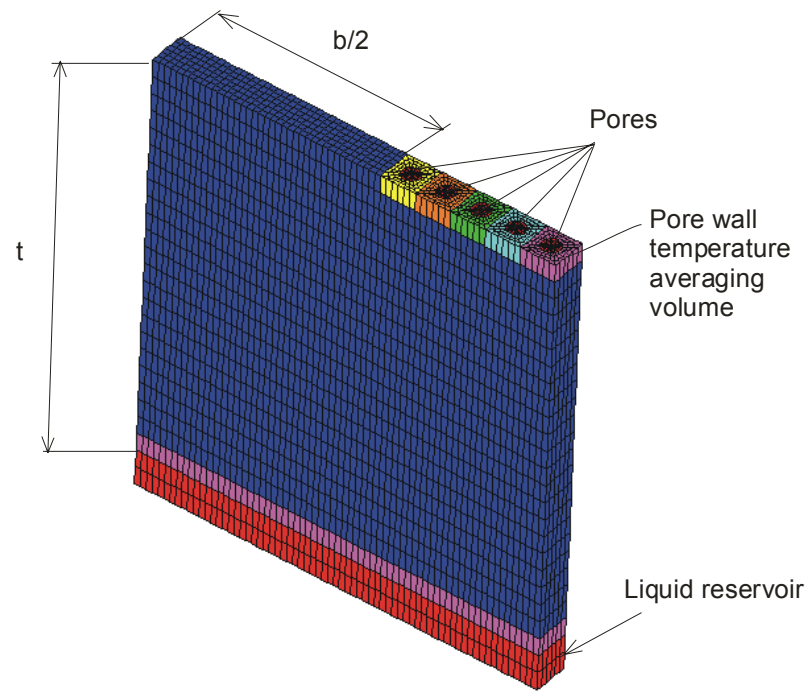
Figure 4.6. Second numerical model nodalization grid

$$q''_{\text{post bottom}} = \frac{q''_{\text{chip}} LW}{Lb} \tag{4.1}$$

$$q''_{\text{pore}} = 38.13505 T_w - 3321.61 \tag{4.2}$$

The adiabatic boundary assumption at the bottom is conservative and gives maximal possible bottom temperature having the highest boiling potential. Separate calculations have been performed for post bottom width, described as parameter b (Figure 4.5), and pore number optimization. Main model parameters are presented in Table 4.2.

Parameter	Value
Bottom post width, μm	20;40;60;100;300
Pore number on the channel width	15
Pore diameter, μm	10
Pitch to diameter ratio	1.5
Chip heat flux, W/cm^2	100

Table 4.2. Post optimization calculation matrix

Post bottom width was varied from 20 μm to 300 μm and pore number has been set at 15 for post optimization. The amount of energy transferred by conduction through the wick depends on the "b" width. Heat flux has been recalculated for each "b" variation. Pore heat flux is set as a function of wick temperature for each b variation.

Closest to the post wick pore wall temperature is higher than any other pore wall temperature as was qualitatively shown in Figure 3.7. The pore at the center of the vapor channel has the maximum distance to the post and therefore minimal wick temperature. The temperature difference between above pore wall temperatures is schematically shown in Figure 4.5 and called ΔT_{pore} later in the text.

ΔT_{pore} is important for total evaporation rate estimation as was qualitatively shown in Figure 3.7. The temperature difference between the porous structure top and bottom is also schematically shown in Figure 4.5 and called $\Delta T_{structure}$. $\Delta T_{structure}$ is important in order to estimate backside boiling. Quantitative estimation of the ΔT_{pore} and $\Delta T_{structure}$ was made on the basis of the second numerical model results.

A higher b value corresponds to higher unit cell post top width and therefore a higher amount of energy transferred to the unit cell. Therefore all geometries converged at different temperatures (Figure 4.7) and a higher b value corresponds to higher final temperature as expected. The operating temperature for b equal to 300 μm exceeds the maximal wick wall temperature and therefore is unacceptable for current geometry.

ΔT_{pore} for the above geometries is presented in Figure 4.8. It has minimal value for a b approximately equal to 70 μm.
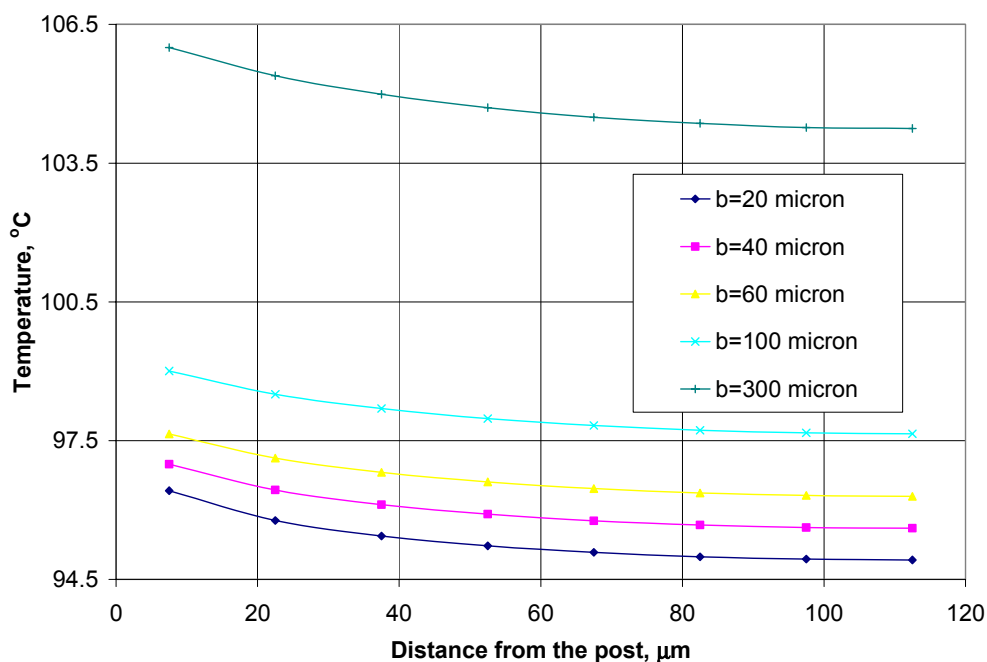
Figure 4.7. Pore wall temperature distribution

ΔT_{pore} is considerably small for range of b values nevertheless it significantly effects evaporation rate since the evaporation rate varies with pore temperature. The

maximal evaporation rate corresponds to maximum wall temperature near the post. The minimal evaporation rate is at the center of the unit cell. The ratio of minimal to maximal evaporation rates as a function of post bottom width is shown in Figure 4.9. One can see that the ΔT_{pore} variation has a minor effect on the evaporation rate ratio over the range of b variation. This can be explained by considering temperature variation between any two geometries. Consider geometry with b equal to 20 μm versus geometry with b equal to 40 μm. The difference between ΔT_{pore} is just 0.1 K whereas difference between close to the post and center pore wall temperatures is 0.5 K (Figure 4.10).
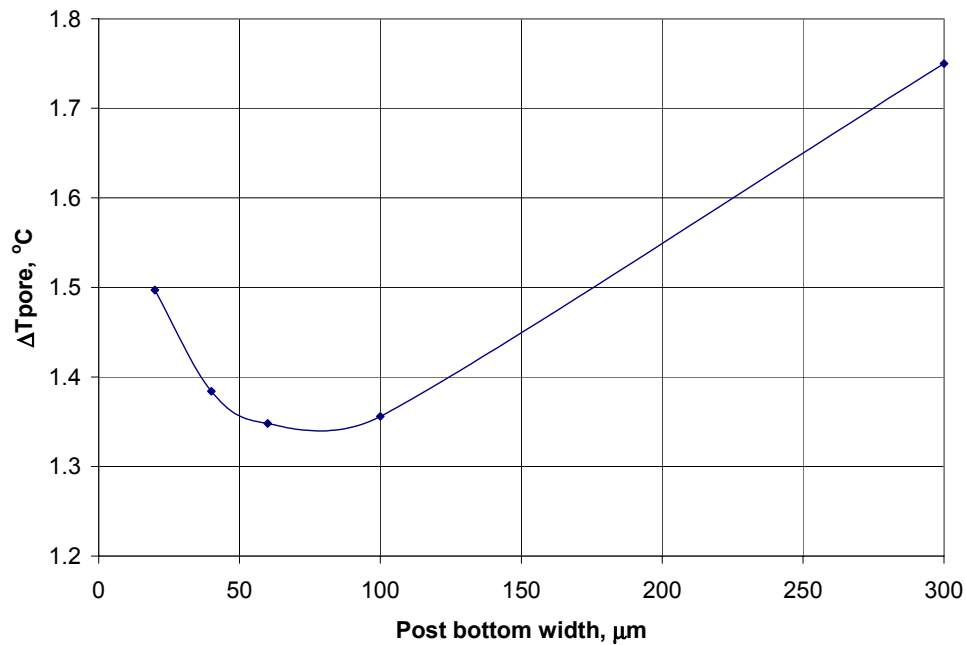
Figure 4.8. Pore wall temperature difference
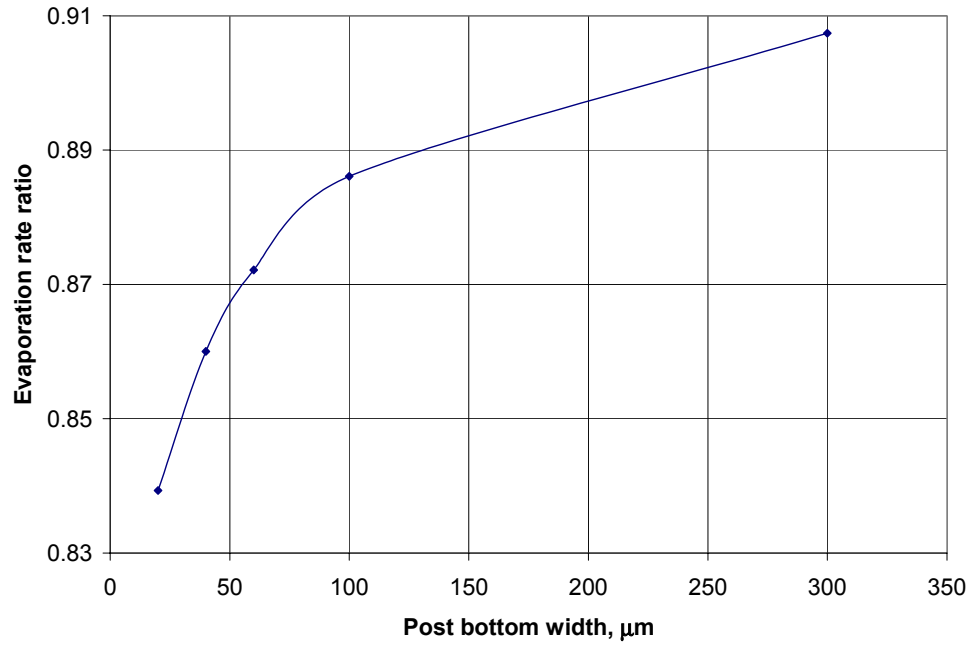
Figure 4.9. Evaporation rate ratio as a function of the post bottom width
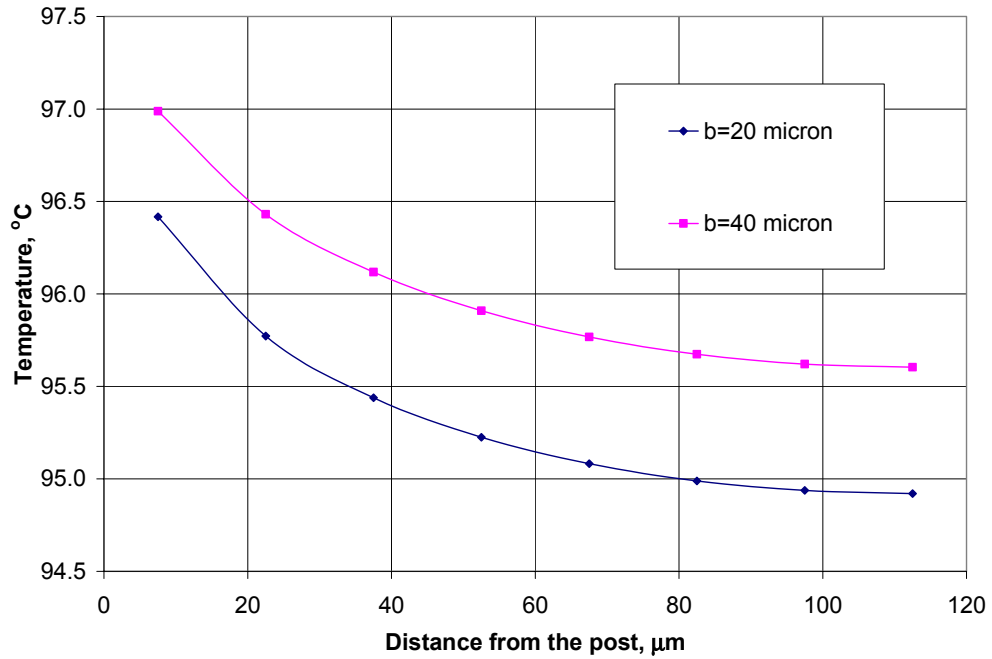
Figure 4.10. Pore wall temperature distribution

One can see that although evaporation rate ratio is increasing with increasing b, which leads to more equal evaporation, operational temperature is also increasing and so is maximum wick temperature, which is undesired from the design goals point of view. Another negative tendency is increased ΔT_{pore} with b increasing, which may cause considerable temperature gradients in the structure.

The difference between porous structure wick top and bottom maximum temperature ($\Delta T_{structure}$) as a function of post bottom width b is shown in Figure 4.11.
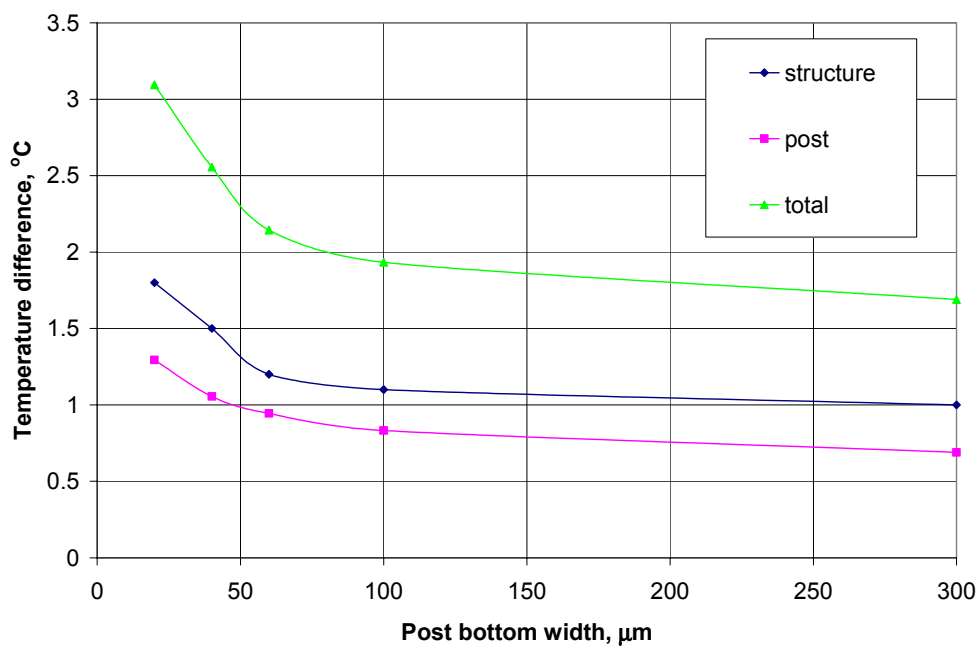
Figure 4.11. Evaporator post and structure temperature differences

One can see that smaller b value corresponds to higher post temperature drop which leads to higher chip surface temperature since power is constant and pore wall temperature must achieve the same value for all geometries to satisfy energy balance limitation. Also smaller b value corresponds to a higher $\Delta T_{structure}$ which leads to lower boiling potential since maximum backside temperature becomes lower.

A maximum b value should be within overall operating limits and minimal ΔT_{pore} on the basis of backside boiling analysis.

The vapor channel width (see Figure 3.6) has been varied by varying the number of pores in order to optimize the pore distribution (Table 4.3).

Parameter	Value
Bottom post width, μm	20
Pore number on the vapor channel width	15;20;30
Vapor channel width, μm	225;300;450
Pore diameter, μm	10
Pitch to diameter ratio	1.5
Chip heat flux, W/cm^2	100

Table 4.3. Pore number optimization calculation matrix

Vapor channel width, which represents a unit cell evaporating width, was changed by applying a different number of pores and keeping pitch to diameter ratio and pore diameter constant. Therefore total unit cell width also changes and so must the amount of energy transferred through the post. A higher vapor channel width corresponds to a higher amount of energy transferred to the unit cell. Although these

changes affect unit cell, total LHP power is constant. Increased unit cell dimensions lead to smaller total number of unit cells. A constant heat flux boundary for the numerical model was recalculated for each pore. Vapor channel width can be expressed ether by length units or by number of pores. It has been found more informative to use the second choice. Parental values can be found in Table 4.3

Pore wall temperature distribution is presented in Figure 4.12. One can see that the larger number of pores and so higher vapor channel width leads to higher temperature difference between neighbor pores and therefore ineffective evaporation. Ratio of minimal to maximal evaporation rates as a function of vapor channel width is shown in Figure 4.13. The above ratio becomes smaller with pore number increasing and achieves 0.1 for pore number of about 72 (this value has been found by extrapolation), which corresponds to vapor channel width of about 1000 μm. A ratio equal to 0.1 means that center pore has 10% of the evaporation rate achieved by pore closest to post.

The difference between maximal top temperature and maximal bottom temperature ($\Delta T_{structure}$) as a function of pore number is shown in Figure 4.14.

One can see that smaller pore number corresponds to lower structure temperature drop, which leads to higher boiling potential since backside temperature is higher. At the same time, a smaller pore number corresponds to a higher evaporation rate per evaporator area as it was shown in Figure 4.13. A minimal value of pore number (and channel width) should be used on the basis of backside boiling analysis.
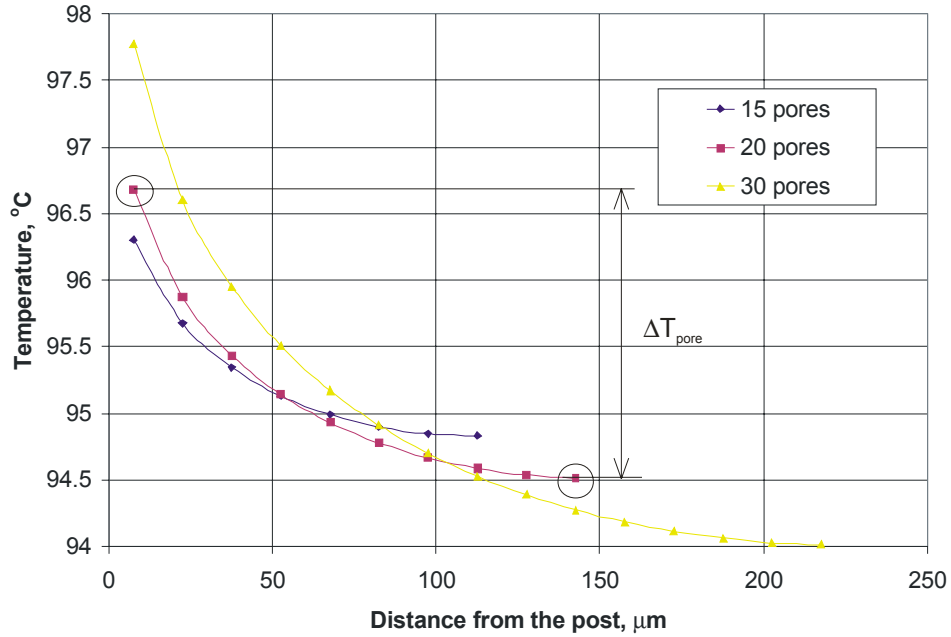
Figure 4.12. Pore wall temperature distribution
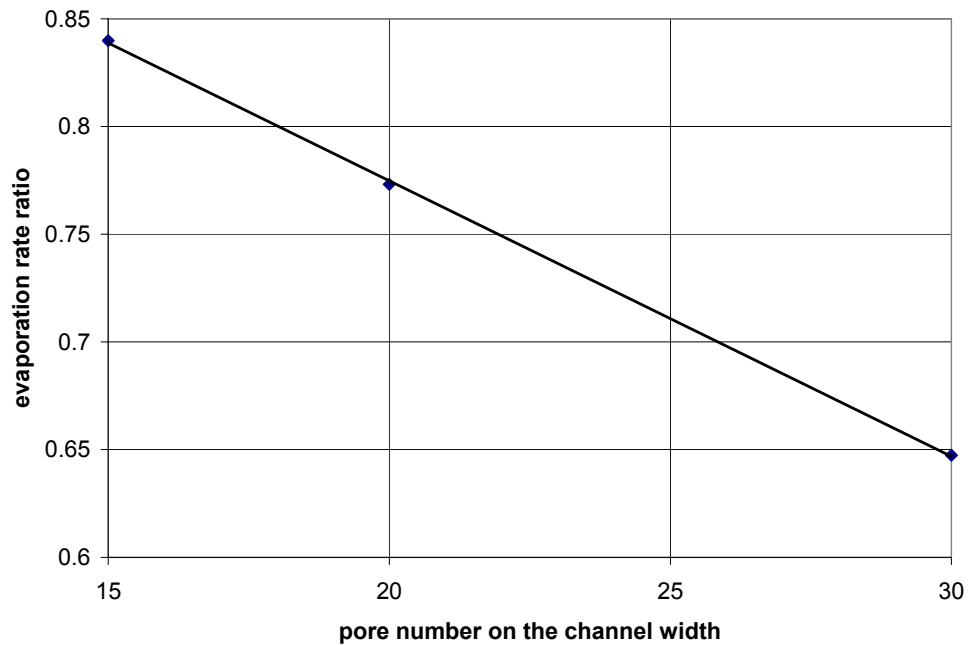
Figure 4.13. Evaporation rate ratio as a function of the vapor channel width
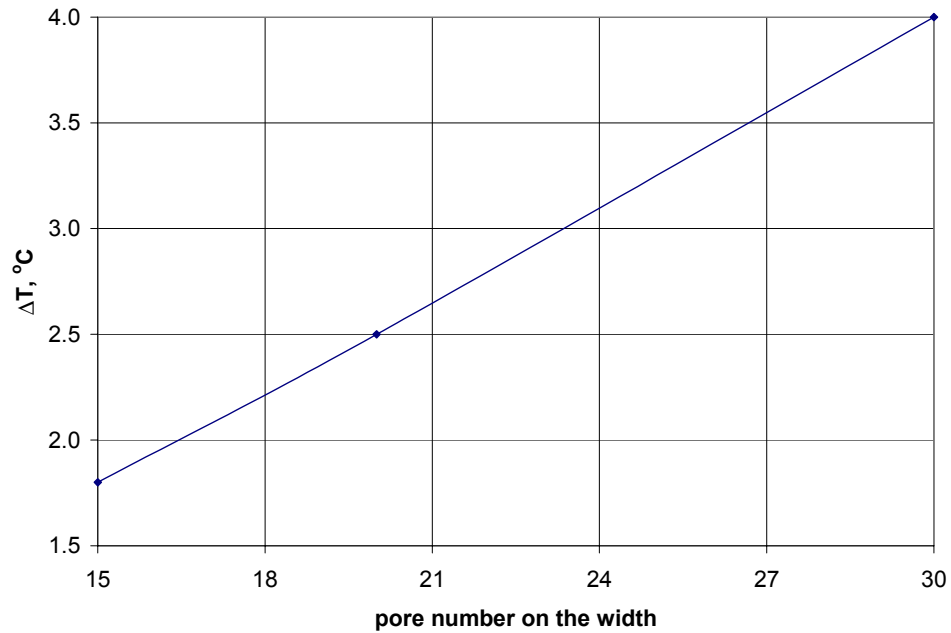
Figure 4.14. Structure temperature difference

The same calculations were performed for a pitch to diameter ratio equal to three. Geometry parameters used are presented in Table 4.4.

Parameter	Value
Channel height, μm	200
Bottom post width, μm	20
Pore number on the vapor channel width	15;20;30
Vapor channel width, μm	450;600;900
Pore diameter, μm	10
Pitch to diameter ratio	3
Chip heat flux, W/cm^2	100

Table 4.4. Pitch to diameter optimization calculation matrix

A similar behavior was found in comparing Figures 4.15-4.17 to Figures 4.12-4.14. The ratio of minimal to maximal evaporation rate (Figure 4.16) has been found to be smaller compare to Figure 4.13 regardless of a higher ΔT_{pore} (Figures 4.15 and 4.12); ΔT_{pore} is found as the difference between maximal and minimal temperature for each pore number as shown in Figure 4.12 for 20 pores on the channel width. This can be explained by a significantly higher evaporation rate per pore area, resulting from the higher energy input compared with the smaller pitch to diameter ratio. Higher energy input is a result of increased unit cell width caused by increased vapor channel width (Table 4.4) A higher structure temperature difference (Figures 4.17 and 4.14) leads to a lower boiling potential although significantly higher top temperature values (Figure 4.18) cause higher bottom temperature values and therefore higher boiling potential compared with smaller pitch to diameter ratio.

Compare Figures 4.15-4.17 to Figures 4.12-4.14 and from above discussion one can see that higher pitch to diameter ratio has no advantages over smaller pitch to diameter ratio. Therefore an evaporator with minimum possible pitch to diameter ratio should be used.
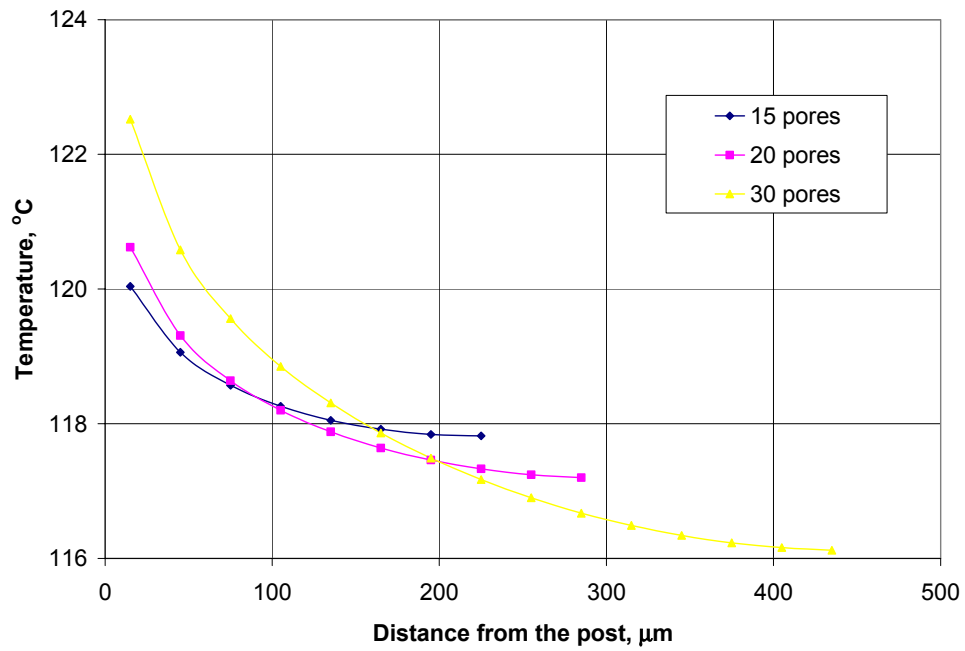
Figure 4.15. Pore wall temperature distribution
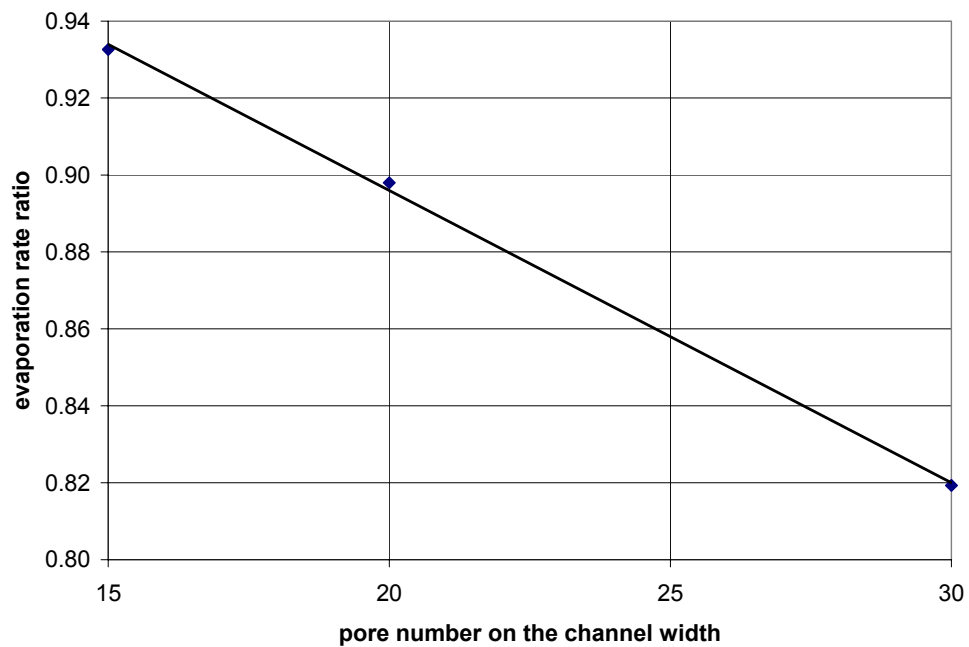
Figure 4.16. Evaporation rate ratio as a function of the vapor channel width
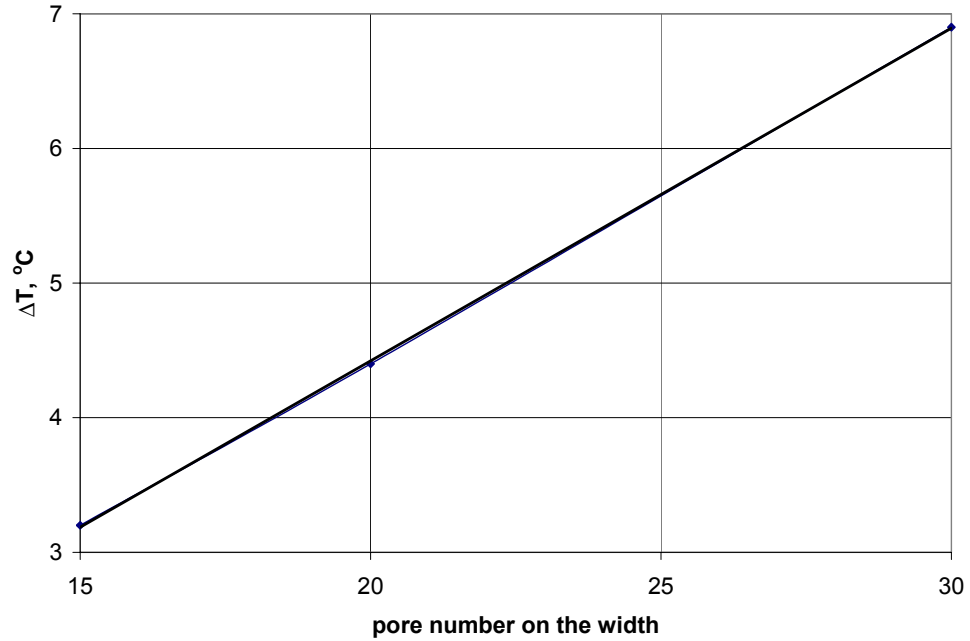
Figure 4.17. Structure temperature difference
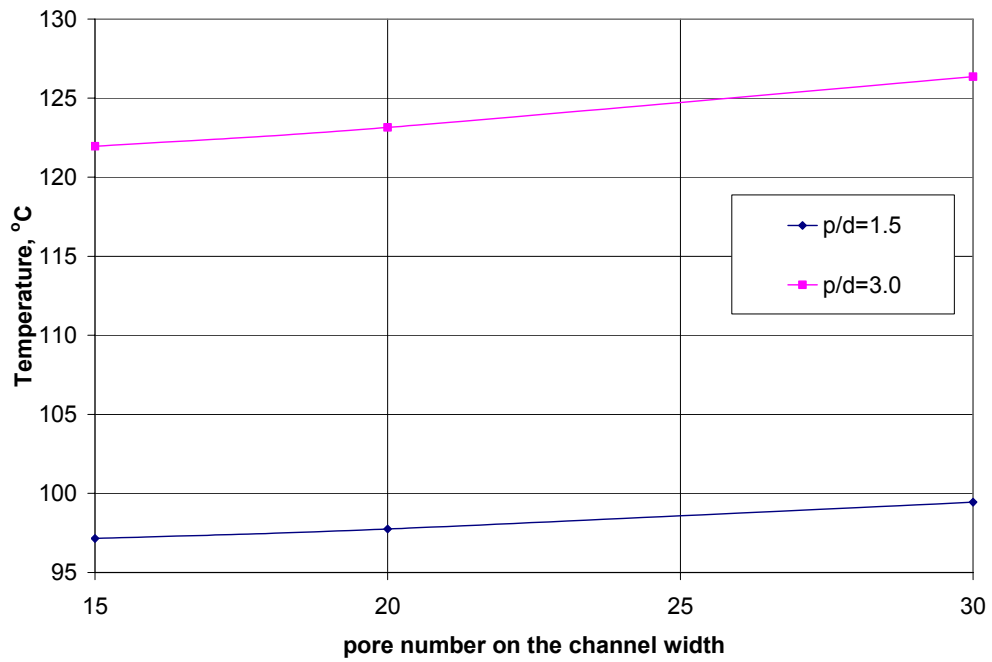
Figure 4.18. Maximum temperature under the post

CHAPTER SUMMARY

A number of recommendations were made for post bottom width and pore number size, and pitch to diameter ratio optimization on the basis of numerical model calculation results.

An evaporator with minimal possible pitch to diameter ratio should be used.

Post bottom width and vapor channel width showed multiple positive and negative tendencies depending on the size change and complicating their optimization. The final optimization of the above parameters is performed on the basis of backside boiling potential, described in the following chapter.

CHAPTER V

BOILING POTENTIAL AND OPTIMAL DESIGN

BOILING POTENTIAL

Evaporation on the back side of the wick is of high importance, since heat pipe operation is impossible in case boiling occurs. A simplified method to estimate back side boiling has been developed based on the first principles evaporation model. The method is based on the assumption that if vapor bubble conditions correspond to a negative evaporation rate, estimated using FPEM, vapor bubble collapses and boiling does not occur. Working fluid parameters, providing negative evaporation rate (i.e. no boiling) for a range of bubble diameters have been chosen as basic parameters for heat pipe optimal design.

The relation of the bubble internal vapor pressure to surrounding liquid pressure can be found from mechanical equilibrium (Carey[8]) for the simplest case of a spherical vapor bubble of pressure P_v with a saturation temperature of T_v in a liquid with pressure P_l, which corresponds to liquid saturation temperature T_{sat}

$$P_v = P_l + \frac{2\sigma}{R_c} \tag{5.1}$$

where σ is the interfacial surface tension and R_c is the bubble radius of curvature. The liquid is assumed to be in thermal equilibrium with the vapor, so liquid temperature is equal to vapor temperature which implies that the liquid temperature is higher than liquid saturation temperature. Liquid temperature and pressure can be found from analytical and numerical calculation of heat pipe conditions. The bubble radius of curvature is assumed to be equal to the bubble radius. The evaporation rate as a function of vapor pressure, liquid temperature and bubble radius has been found using FPEM for pore evaporation assuming liquid temperature equal to pore wall temperature, and bubble radius as a pore radius. Evaporation rate for number of parameters is presented in Table 5.1.

P_{liquid}, Pa	d,m	T_{sat}, ^oC	P_{vapor}, Pa	Evaporation rate, $T_{liquid}=95^oC$	P_{vapor}, Pa	Evaporation rate, $T_{liquid}=84^oC$
80000	$1.0*10^{-6}$	93.49	315520.00	negative	328600.00	negative
80000	$5.0*10^{-6}$	93.49	127104.00	negative	129720.00	negative
80000	$1.0*10^{-5}$	93.49	103552.00	negative	104860.00	negative
70000	$1.0*10^{-6}$	89.93	305520.00	negative	318600.00	negative
70000	$5.0*10^{-6}$	89.93	117104.00	negative	119720.00	negative
70000	$1.0*10^{-5}$	89.93	93552.00	negative	94860.00	negative
50000	$1.0*10^{-6}$	81.32	285520.00	negative	298600.00	negative
50000	$5.0*10^{-6}$	81.32	97104.00	negative	99720.00	negative
50000	$1.0*10^{-5}$	81.32	73552.00	positive	74860.00	negative
30000	$1.0*10^{-6}$	69.13	265520.00	negative	278600.00	negative
30000	$5.0*10^{-6}$	69.13	77104.00	positive	79720.00	negative
30000	$1.0*10^{-5}$	69.13	53552.00	positive	54860.00	positive

Table 5.1. Evaporation rate estimation for 95°C and 84°C liquid temperatures

One can see that higher liquid superheat gives higher chance of positive evaporation rate and so backside boiling. Smaller diameter bubbles have a lower chance of existence. Therefore it seems reasonable to choose geometry with smaller pore diameter and having smaller total pressure drop so liquid pressure at the evaporator backside would be higher. Evaporation rate for bubble diameter of 1 μm is presented in Figure 5.1.
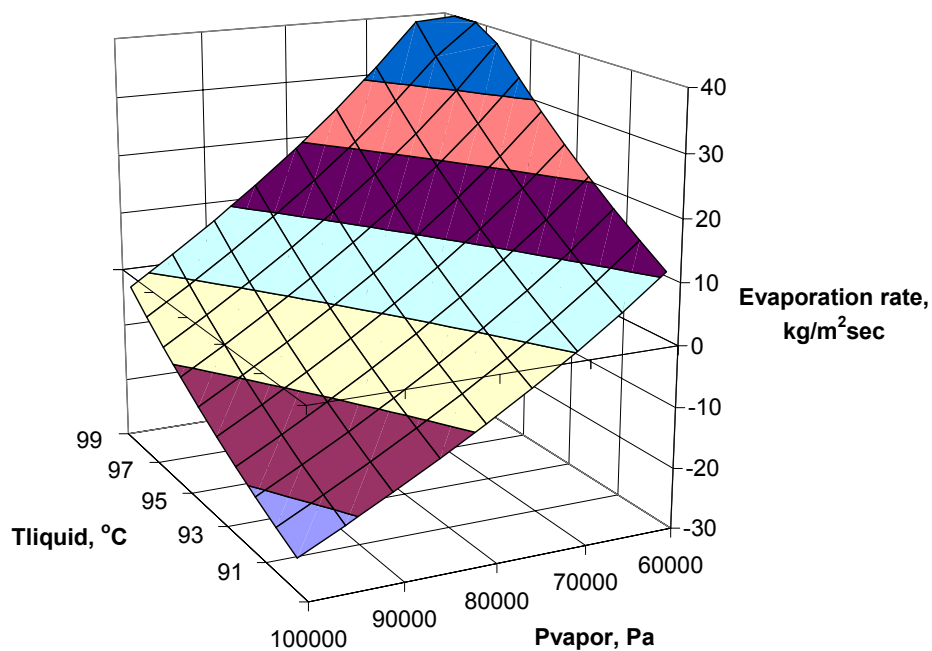
Figure 5.1. Evaporation rate estimation for bubble radius of 1 μm

Maximal heat pipe pressure calculations are described in Chapter III. It varies from 95000 Pa to 85000 Pa, depending on post temperature drop, for described geometries. One can see from Table 5.1 that evaporation rate has positive value for liquid pressure of 50000 Pa and below. Therefore this pressure can be conservatively

assumed as minimal heat pipe operating pressure. The difference between the lowest of maximal heat pipe pressures and assumed minimal heat pipe operating pressure gives 35000 Pa as a maximal allowed heat pipe total pressure drop.

OPTIMAL DESIGN

The optimal design has been found taking into account all analytical, numerical, and FPEM model results.

Analysis performed in Chapter III showed that a pore of 1 μm and lower has better chance to satisfy pressure and heat balance limitation. Set of analytical calculation has been performed to define optimal geometry parameters for pore diameters of 1.0 and 0.5 μm. Figures 5.2 and 5.3 represent FPEM evaporation rate, expressed in terms of heat flux, and the heat flux necessary to balance input energy for 1 μm and 0.5 μm pore diameters. One can see that a number of geometries satisfy the energy balance limitation within the estimated post height range. Higher post height corresponds to higher channel width and lower vapor pressure drop as was previously described. Minimal channel (and unit cell) width should be sought in order to maximize pore evaporation according to recommendations given in Chapter IV. The final design decision was made on the basis of results presented in Figures 5.4 and 5.5 where geometries satisfying the energy balance limitation are circled.
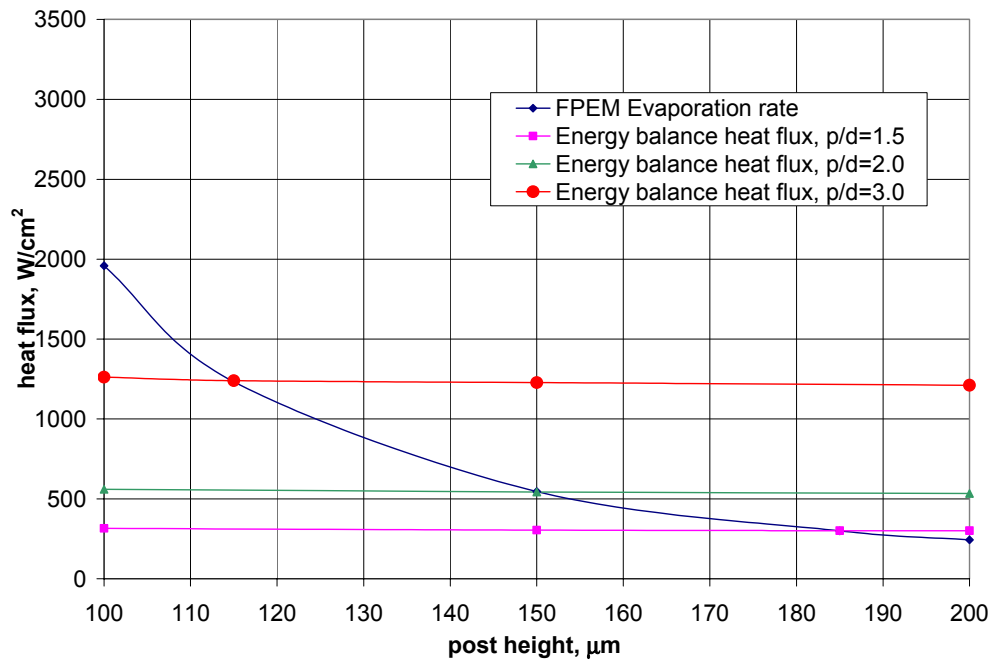
Figure 5.2. Heat flux comparison for 1.0 µm pore diameter
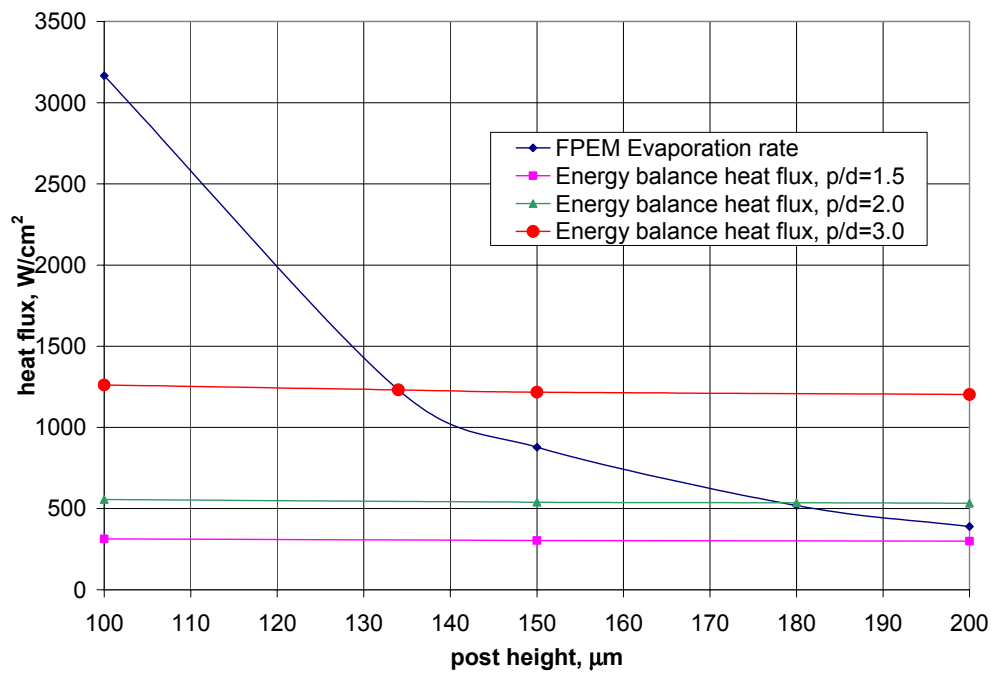
Figure 5.3. Heat flux comparison for 0.5 µm pore diameter
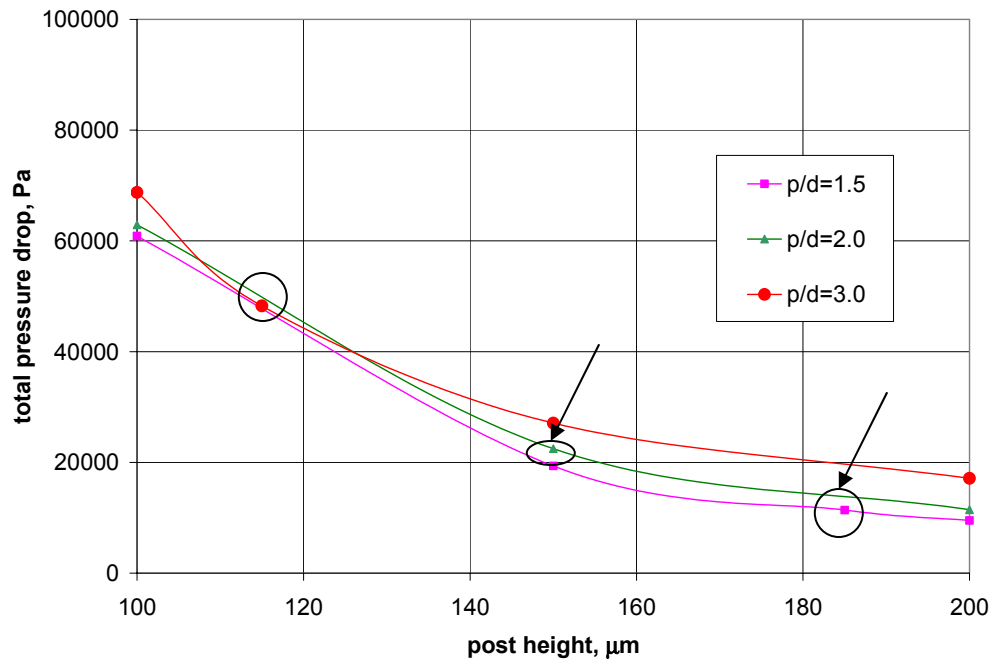
Figure 5.4. Total pressure drop as a function of post height for 1.0 µm pore diameter
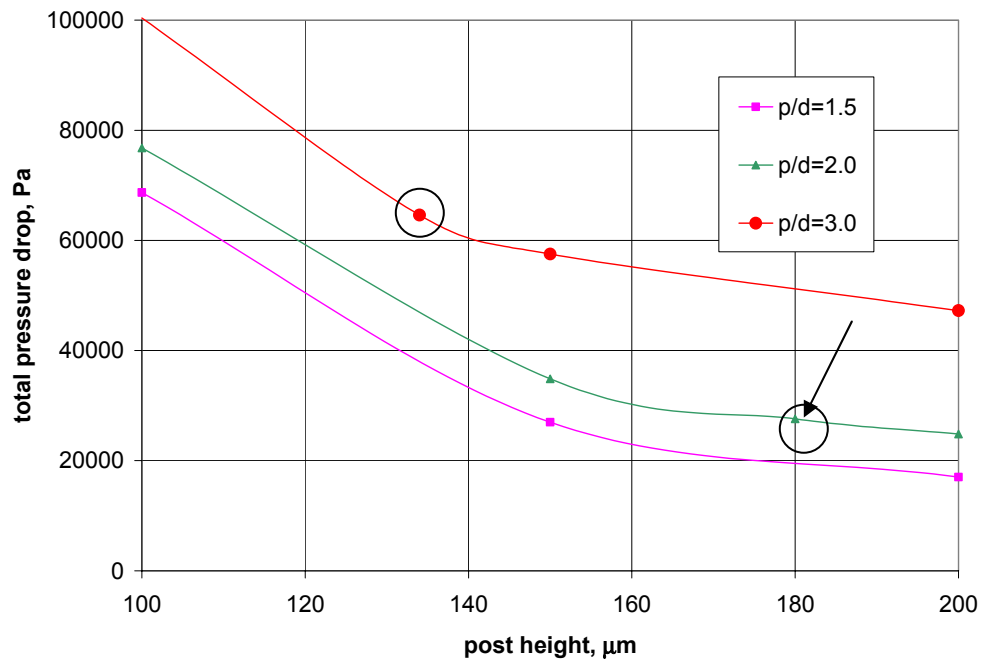
Figure 5.5. Total pressure drop as a function of post height for 0.5 µm pore diameter

A pitch to diameter ratio equal to 1.5 at a 0.5 μm pore diameter, which satisfies energy balance limitation at post height exceeding 200 μm, was not considered due to significant evaporation rate difference.

Minimal total pressure drop should be sought on the basis of backside model results. As mentioned in Chapter II, based on heat pipe operating parameters, total temperature drop should not exceed 10 K (10°C). Therefore total pressure drop should not exceed 30000 Pa (see Figure 2.7), which is a more strict requirement than that based on backside calculation. Three geometries, marked by arrows (see Figure 5.4 and 5.5) satisfy this pressure drop requirement. The one with channel height of 150 μm, pitch to diameter ratio of 2.0 and pore diameter of 1 μm was chosen as having minimal channel height and therefore channel width (Figure 5.4). Minimal channel width leads to small ΔT_{pore} and therefore equal pore evaporation on channel width. Geometry parameters are presented in Tables 5.2 and 5.3 as preliminary optimal design.

Parameters	Preliminary design	Optimal design
Pore diameter, μm	1	1
h, μm	150	148.95
t , μm	200	200
b, μm	10	10
Pitch/d ratio	2	2
Pore # on the width	86	86
Total pore#	429914	429914

Table 5.2. Preliminary vs. optimal design parameters

Pressure drop			
Working fluid	Place	Value, Pa	Value, Pa
Vapor	Transport line	1136.49	1136.49
Liquid	Transport line	16.63	16.63
Liquid	Pore	4535.63	4505.80
Vapor	Vapor channel	16784.68	17146.50
Total		22473.44	22805.44
Capillary limit		235520.00	235520.00
Thermodynamic pressure limit		88297.68	88297.68

Table 5.3. Preliminary vs. optimal design pressure drop values

The evaporator temperature distribution was found on the basis of a numerical calculation identical to the second numerical model, described in Chapter IV. The preliminary design does not take into account evaporator temperature distribution (see Figure 3.7) and is based on the assumption that all pore wall temperatures are equal to the temperature under the post, as described in Chapter III. Therefore actual FPEM evaporation rate is lower than estimated analytically. This leads to higher operating temperature and is undesirable. One can see from Figure 5.4 that a higher evaporation rate can be achieved for smaller channel width. Analytical and numerical calculations have been repeated for a number of smaller channel widths until the maximal operating temperature became equal to maximal design temperature.

A negative effect of smaller channel width is increased vapor and total pressure drop, nevertheless both channel width and pressure change are insignificant as it can be seen in Table 5.2, where the optimal design is compared to preliminary design.

The optimal design vapor channel temperature distribution is shown in Figure 5.6. One can see that maximal temperature value under the post is 370.1 K, center pore wall temperature is 368.6 K, backside temperature is 368.8 K. Backside temperature is somewhat overestimated, since adiabatic boundary at the bottom has been applied.
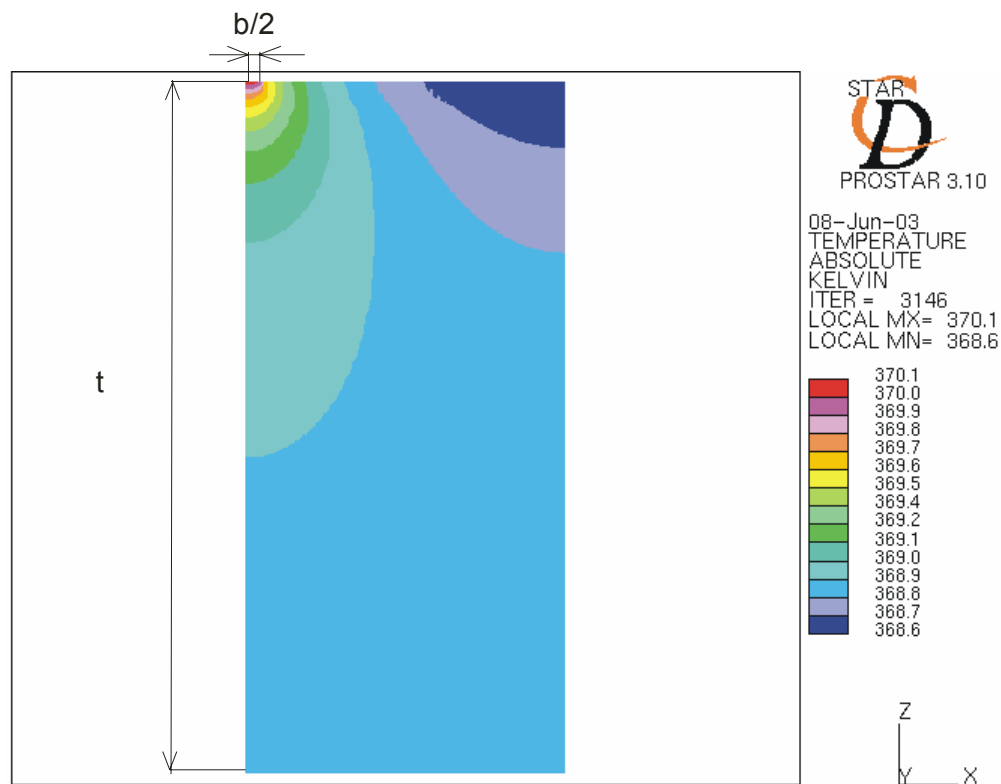
Figure 5.6. Optimal design evaporator temperature distribution

The optimal design's thermodynamic cycle is presented in Figure 5.7. The maximum temperature difference is less than $7^{o}C$, which is within limits.

Thus optimal design is adequate for all imposed constrains and proposed for experimental investigation.
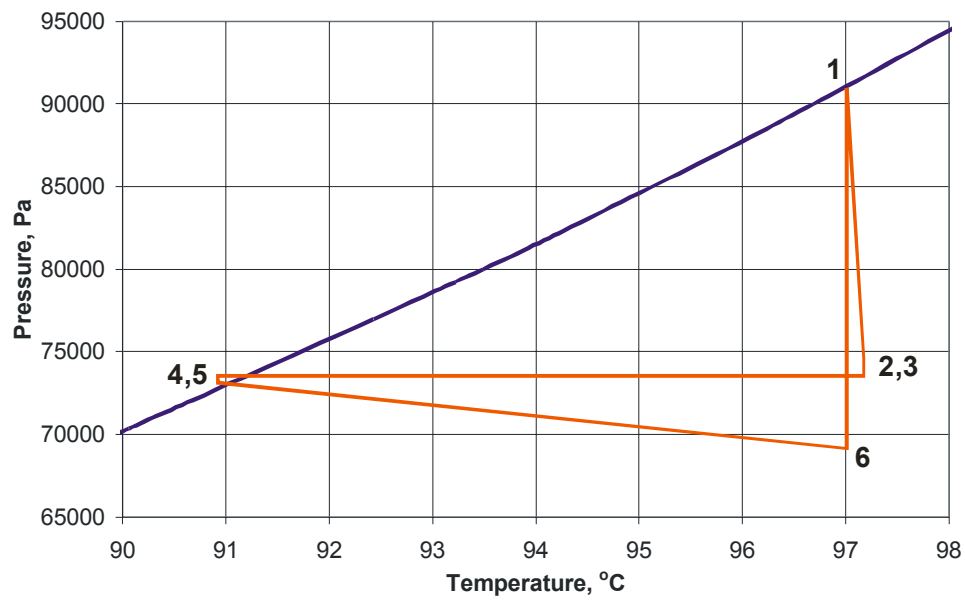
Figure 5.7. Optimal design thermodynamic cycle

CHAPTER SUMMARY

This chapter describes boiling potential estimation and design optimization. Boiling potential limitations are found to be less strict that described in Chapter III heat pipe operating temperature difference limit.

An iterative process, based on analytical and numerical calculations, to optimize loop heat pipe evaporator geometry has been applied. The proposed design meets all known limitations and design goals.

CHAPTER VI

SUMMARY AND RECOMMENDATIONS

SUMMARY

A silicon evaporator with a coherent pore structure has been proposed for a conceptual loop heat pipe design in Chapter I. Evaporator fabrication is performed by using photo-lithographic fabrication technology. A previously developed first principles evaporation model has been simplified for engineering calculations of pore evaporation rate. It has been found that the above model can be presented as a function of pore wall temperature, vapor pressure and pore radius. A smaller diameter pore can achieve a significantly higher evaporation rate as described in Chapter II. Analytical calculation of pressure drop, energy balance and post temperature distribution is described in Chapter III.

A number of classical heat pipe limitations have been described and their importance for the proposed design has been evaluated. New limitations, based on design goals were introduced. Numerical calculations, described in Chapter IV, were performed to optimize the evaporator temperature distribution since existing analytical models have been found either overly complicated or inapplicable. A number of recommendations have been given on the basis of the numerical model results. Some phenomena have opposing impacts on the design. Backside boiling potential estimation

has been performed and included in optimal design. A series of calculations have been performed in order to optimize the concept loop heat pipe design. The optimal design meets all known limitations and design goals.

A new heat pipe calculation method, combining classical limitations, first principles evaporation rate estimation, and numerical modeling has been developed.

The method can be summarized as follows:

a) temperature distribution calculation

b) analytical calculation of total pressure drop and comparison with capillary pressure rise

c) analytical energy balance calculation

d) FPEM evaporation rate calculation and comparison with energy balance calculation

e) thermodynamic cycle construction and comparison with maximal operating pressure drop limitation

f) numerical evaporator temperature distribution calculation and comparison with desired operating parameters.

Although the geometry optimization recommendations, given in Chapter IV, can be applied to the described conceptual geometry only, they can be used for optimization using working fluid other than water. The developed iteration method can generally be applied for any loop heat pipe calculation.

RECOMMENDATIONS

A series of experiments needs to be conducted to evaluate the optimal design and FPEM results.

Reliable data for silicon-water interface contact angle at the pore diameter range of interest are necessary for further optimization.

REFERENCES

1.   C. A. WARD and G. FANG, "Expression for Predicting Liquid Evaporation Flux: Statistical Rate Theory Approach", *Physical Review,* E 59, 429, (1999).

2.   R. OINUMA, "First Principles Evaporation Modeling in Porous Media", Ph. D. Dissertation, Texas A&M University, College Station, (to be submitted).

3.   G. P. PETERSON, *An Introduction to Heat Pipes*, John Wiley & Sons, Inc., New York, (1994).

4.   D. M. ERNST, A. L. PHILIPS (FRED) and I. S. ROZIN, "Loop Heat Pipes – Their Potential", Proceedings of the IX International Heat Pipe Conference, Albuquerque, New Mexico, (1995).

5.   R. RICHTER and J. M. GOTTSCHLICH, "Thermodynamic Aspects of Heat Pipe Operation", *Journal of Thermophysics and Heat Transfer*, 8 (2), 334, (April-June 1994).

6.   M. HAMDAN, D. CYTRYNOWICZ, P. MEDIS, A. SHUJA, F. M. GERNER, H. T. HENDERSON, E. GOLLIHER, K. MELLOTT and C. MOORE, "Loop Heat Pipe (LHP) Development by Utilizing Coherent Porous Silicon (CPS) Wicks", ITHERM International Conference on Thermal Phenomena in Electronic Systems, San Diego, California, (May 29 – June 1, 2002).

7.   *ASME Steam Properties for Industrial Use Based on IAPWS-IF97*, Professional Version, Three Park Avenue, New York, (1998).

8.   V. P. CAREY, *Liquid-Vapor Phase-Change Phenomena: An Introduction to the Thermophysics of Vaporization and Condensation Process in Heat Transfer Equipment*, Taylor & Francis, Hebron, Kentucky, (1992).

9.   M. F. WHITE, *Viscous Fluid Flow*, McGraw-Hill, Inc., New York, (1991).

10.   F. P. INCROPERA and D. P. DEWITT, *Fundamentals of Heat and Mass Transfer*, 4th edition, John Wiley & Sons, New York, (1996).

11.   A. F. MILLS, *Heat Transfer*, Prentice Hall, Upper Saddle River, New Jersey, (1999).

12. M. N. IVANOVSKII, V. P. SOROKIN and I.V. YAGODKIN, *The Physical Principles of Heat Pipes*, Clarendon, Oxford, England, (1982).

13. YU. F. MAIDANIK, YU. G. FERSHTATER and K. A. GONCHAROV, "Capillary-Pump Loop for the Systems of Thermal Regulation of Spacecraft", 4th European Symposium on Space Environmental and Control Systems, Florence, Italy, (21-24 October, 1991), ESA SP-324.

14. J. T. DICKEY and G. P. PETERSON, "An Experimental and Analytical Investigation of the Operational Characteristics of a Capillary Pumped Loop", AIAA 28th Thermophysics Conference, Orlando, FL, (6-9 July, 1993), AIAA 93-2746.

15. T. J. LACLAIR and I. MUDAWAR, "Thermal Transients in a Capillary Evaporator Prior to the Initiation of Boiling", *International Journal of Heat and Mass Transfer*, 43 (21), 3937, (November 2000).

16. V. PLATEL, C. BUTTO, J. GRANDPEIX and J. JOLY, "Detailed Modelling of the Evaporator of a Capillary Pumped Loop", *Revue Générale de Thermique*, 35 (415), 434, (July 1996).

17. M. P. MUGHAL and O. A. PLUMB, "An Experimental Study of Boiling on a Wicked Surface", *International Journal of Heat and Mass Transfer*, 39 (4), 771, (March 1996).

18. D. A. PRUZAN, L. K. KLINGENSMITH, K. E. TORRANCE and C. T. AVEDISIAN, "Design of High-Performance Sintered-Wick Heat Pipes", *International Journal of Heat and Mass Transfer*, 34 (6), 1417, (June 1991).

19. D. A. PRUZAN, K. E. TORRANCE and C. T. AVEDISIAN, "Two-Phase Flow and Dryout in a Screen Wick Saturated with a Fluid Mixture", *International Journal of Heat and Mass Transfer*, 33 (4), 673, (April 1990).

20. R. PONNAPPAN, M. L. RAMALINGAM, J. E. JOHNSON and E. T. MAHEFKEY, "Evaporator Critical Heat flux in the Double-Wall Artery Heat Pipe", *Experimental Thermal and Fluid Science*, 2 (4), 450, (October 1989).

21. K. H. SUN and C. L. TIEN, "Thermal Performance Characteristics of Heat Pipes", *International Journal of Heat and Mass Transfer*, 18 (3), 363, (March 1975).

22.   J. KU, "Thermodynamic Aspects of Capillary Pumped Loop Operation", 6th AIAA/ASME Joint Thermophysics and Heat Transfer Conference, Colorado Springs, Colorado, (20-23 June, 1994), AIAA 94-2059.

23.   A. BRAUTSCH and P. A. KEW, "Examination and Visualization of Heat Transfer Processes During Evaporation in Capillary Porous Structures", *Applied Thermal Engineering*, 22 (7), 815, (May 2002).

APPENDIX 1

FPEM CONSTANTS

Constant	Value
N_A, molecules/mol	$6.024 * 10^{23}$
Θ_1, K	2290
Θ_2, K	5160
Θ_3, K	5360
k, J/K molecule	$1.380 * 10^{-23}$
m, kg/mol	$18.0 * 10^{-3}$

APPENDIX 2

PROGRAM "EVAPORATOR"

```fortran
!  program.f90
!
!

!*************************************************************************
! Evaporator optimization
!*************************************************************************

        program evaporator
        implicit none

        integer numw,numl,numtot,flag1,i

        double precision pi,hfg,sigma,mul,rol,muv,rov,k,lvtr,lltr,dvtr,dltr,Achip,L,d,t,h,b
        double precision Ptotmax,q11chip,W,p,Aevap,dPcap,dPvaptr,dPliqtr,mdottot,mdotpore
        double precision Vlp,Relp,f,dPliquid,Atr,Vv,dh,CfRe,Rev,dPvapor,dPtotal,dTcw,q11poreR
        double precision pdratio,Paverage,Ttop,Tevap,q11poreN,Asat,numtotsat,pitchsat
        double precision pdratiosat,dPtotmax
        double precision Tchip,T6,PsatT6,PsatTc
        pi=3.14159265

!!!!!!!!!!!!!!!!!!!!!!!!!!!!!!!!!!!!!!!!!!!!!!!!!!!!!!!!!!!!!!!!!!!!!!!!!!!!!!!!!!!!!!!!!!!!
! Flags
!!!!!!!!!!!!!!!!!!!!!!!!!!!!!!!!!!!!!!!!!!!!!!!!!!!!!!!!!!!!!!!!!!!!!!!!!!!!!!!!!!!!!!!!!!!!

!        flag1=0

!!!!!!!!!!!!!!!!!!!!!!!!!!!!!!!!!!!!!!!!!!!!!!!!!!!!!!!!!!!!!!!!!!!!!!!!!!!!!!!!!!!!!!!!!!!!
! Liquid properties (Water, T=100 degrees C)
!!!!!!!!!!!!!!!!!!!!!!!!!!!!!!!!!!!!!!!!!!!!!!!!!!!!!!!!!!!!!!!!!!!!!!!!!!!!!!!!!!!!!!!!!!!!

!        teta=40

        hfg=2256.00e3                           ! latent heat of evaporization, J/kg

        sigma=5.888e-2                          ! surface tension, N/m

        mul=2.824e-4                            ! liquid viscosity, Pa*sec (kg/m*sec)

        rol=958.37                              ! liquid density, kg/m**3

        muv=1.204e-5                            ! vapor viscosity, Pa*sec (kg/m*sec)

        rov=0.5979                              ! vapor density, kg/m**3
```

```
!!!!!!!!!!!!!!!!!!!!!!!!!!!!!!!!!!!!!!!!!!!!!!!!!!!!!!!!!!!!!!!!!!!!!!!!!!!!!!!!!!!!!!!!!!!!!
! Solid properties (Silicon)
!!!!!!!!!!!!!!!!!!!!!!!!!!!!!!!!!!!!!!!!!!!!!!!!!!!!!!!!!!!!!!!!!!!!!!!!!!!!!!!!!!!!!!!!!!!!!

        k=148
        ! solid conductivity, W/m*K

!!!!!!!!!!!!!!!!!!!!!!!!!!!!!!!!!!!!!!!!!!!!!!!!!!!!!!!!!!!!!!!!!!!!!!!!!!!!!!!!!!!!!!!!!!!!!
! Geometry parameters
!!!!!!!!!!!!!!!!!!!!!!!!!!!!!!!!!!!!!!!!!!!!!!!!!!!!!!!!!!!!!!!!!!!!!!!!!!!!!!!!!!!!!!!!!!!!!

        lvtr=0.5                              ! vapor transport line length, m

        lltr=0.5                              ! liquid transport line length, m

        dvtr=5.0e-3                           ! vapor transport line diameter, m

        dltr=5.0e-3                           ! liquid transport line diameter, m

        Achip=1e-4                            ! chip area, m2

        L=1.0d-2                              ! cell length, m

        d=5.0e-6                              ! pore diameter, m

        t=200.0e-6                            ! pore height, m

!!!!! parameters to change

        h=148.9563695d-6                      ! post height, m
        b=10.0d-6                             ! post bottom width, m
        pdratio=1.5d0                         ! pitch over diameter ratio

!!!!!!!!!!!!!!!!!!!!!!!!!!!!!!!!!!!!!!!!!!!!!!!!!!!!!!!!!!!!!!!!!!!!!!!!!!!!!!!!!!!!!!!!!!!!!
! Thermodynamic limitations
!!!!!!!!!!!!!!!!!!!!!!!!!!!!!!!!!!!!!!!!!!!!!!!!!!!!!!!!!!!!!!!!!!!!!!!!!!!!!!!!!!!!!!!!!!!!!

        Ttop=100.0+273.15                     ! maximal post top temperature, K

        q11chip=1000000.0                     ! q chip double prime, W/m**2

!!!!!!!!!!!!!!!!!!!!!!!!!!!!!!!!!!!!!!!!!!!!!!!!!!!!!!!!!!!!!!!!!!!!!!!!!!!!!!!!!!!!!!!!!!!!!
! Calculation start
!!!!!!!!!!!!!!!!!!!!!!!!!!!!!!!!!!!!!!!!!!!!!!!!!!!!!!!!!!!!!!!!!!!!!!!!!!!!!!!!!!!!!!!!!!!!!

!!!!!!!!!!!!!!!!!!!!!!!!!!!!!!!!!!!!!!!!!!!!!!!!!!!!!!!!!!!!!!!!!!!!!!!!!!!!!!!!!!!!!!!!!!!!!
! Geometry data
!!!!!!!!!!!!!!!!!!!!!!!!!!!!!!!!!!!!!!!!!!!!!!!!!!!!!!!!!!!!!!!!!!!!!!!!!!!!!!!!!!!!!!!!!!!!!

        W=(2.0*h*tan(pi/6.0))+b               ! cell width, m

                                              ! value for the right triangle case only

        p=pdratio*d                           ! pitch, m
```

```fortran
        numw=((W-b)/p)                              ! pore number on the width

        numl=(L/p)-0.5                              ! pore number on the length

        if(pdratio.lt.1.5)then
                print*,"p/d less than 1.5"
                stop
        endif

        numtot=numw*numl                            ! total pore number

        Aevap=numtot*((pi*d*d)/4.0)                 ! total evaporation area, m2

!!!!!!!!!!!!!!!!!!!!!!!!!!!!!!!!!!!!!!!!!!!!!!!!!!!!!!!!!!!!!!!!!!!!!!!!!!!!!!!!!!!!!!!!!!!
! Temperature diference between post top and post bottom
!!!!!!!!!!!!!!!!!!!!!!!!!!!!!!!!!!!!!!!!!!!!!!!!!!!!!!!!!!!!!!!!!!!!!!!!!!!!!!!!!!!!!!!!!!!

!       delta Tcw triangle, K

        dTcw=(q11chip*W*h*log(b/W))/(k*(b-W))

!!!!!!!!!!!!!!!!!!!!!!!!!!!!!!!!!!!!!!!!!!!!!!!!!!!!!!!!!!!!!!!!!!!!!!!!!!!!!!!!!!!!!!!!!!!
! Thermodynamic limitations
!!!!!!!!!!!!!!!!!!!!!!!!!!!!!!!!!!!!!!!!!!!!!!!!!!!!!!!!!!!!!!!!!!!!!!!!!!!!!!!!!!!!!!!!!!!

        Tchip=100
        ! Chip surface temperature, C

        T6=Tchip-dTcw                               !Temperature at point 6, C

        PsatT6=0.01029356*(T6**3.496321)            ! Saturation pressure for

                                                    ! temperature T6, Pa

        PsatTc=2300                                 ! Saturation pressure for condenser

                                                    ! temperature, Pa

        dPtotmax=PsatT6-PsatTc                      ! Maximal total pressure drop, Pa

                                                    ! from thermodynamic consideration

        Ptotmax=PsatT6
!!!!!!!!!!!!!!!!!!!!!!!!!!!!!!!!!!!!!!!!!!!!!!!!!!!!!!!!!!!!!!!!!!!!!!!!!!!!!!!!!!!!!!!!!!!
! Pressure drop calculation
!!!!!!!!!!!!!!!!!!!!!!!!!!!!!!!!!!!!!!!!!!!!!!!!!!!!!!!!!!!!!!!!!!!!!!!!!!!!!!!!!!!!!!!!!!!

!       capillary dP *********************************************************************

        dPcap=(4.0*sigma)/d

!       dPcap=(4.0*sigma*cos((teta*pi)/180.0))/d

!       dP vapor in the transport line ************************************************

        dPvaptr=(32.0*muv*lvtr*4.0*q11chip*Achip)/((dvtr**4.0)*hfg*rov*pi)
```

```
!        dP liquid in the transport line ********************************************************
         dPliqtr=(32.0*mul*lltr*4.0*q11chip*Achip)/((dltr**4.0)*hfg*rol*pi)

!        dP liquid in the pore, Pa *********************************************************
         mdottot=((q11chip*L*W)/hfg)              ! Total mass flow rate kg/sec
         mdotpore=mdottot/(numtot*1.0)            ! Pore mass flow rate, kg/sec
         Vlp=(4.0*mdotpore)/(pi*d*d*rol)          ! Pore liquid velosity, m/sec
         Relp=(rol*d*Vlp)/mul                     ! Pore liquid Reinolds #
         f=64.0/Relp                              ! Friction factor
         dPliquid=f*(t/d)*rol*((Vlp*Vlp)/2.0)
         print*,"Vlp",Vlp

!        vapor channel dP calculation ***********************************************************
         Atr=(h*(W-b))/2.0                        ! Triangle cross sectional area, m2
         Vv=mdottot/(rov*Atr)                     ! Vapor channel velocity, m/sec
         dh=(2.0/3.0)*h                           ! Equivalent hydraulic diameter, m
         CfRe=13.33333                            ! Friction coefficient*Re#
         Rev=(rov*dh*Vv)/muv                      ! Vapor channel Reinolds #
         f=(4.0*CfRe)/Rev                         ! Friction factor
         dPvapor=f*((L/2.0)/dh)*rov*((Vv*Vv)/2.0)

!        total dP ****************************************************************************
         dPtotal=dPvaptr+dPliqtr+dPliquid+dPvapor

         if(dPtotal.gt.dPcap)then
                 print*,"Total dP more than capillary dP"
!                goto 10
         endif
         if(dPtotal.gt.dPtotmax)then
                 print*,"Total dP more than maximal dP"
!                goto 10
         endif

         Paverage=Ptotmax-(dPvapor/2.0)


!!!!!!!!!!!!!!!!!!!!!!!!!!!!!!!!!!!!!!!!!!!!!!!!!!!!!!!!!!!!!!!!!!!!!!!!!!!!!!!!!!!!!!!!!!!!!!
! Heat balance
!!!!!!!!!!!!!!!!!!!!!!!!!!!!!!!!!!!!!!!!!!!!!!!!!!!!!!!!!!!!!!!!!!!!!!!!!!!!!!!!!!!!!!!!!!!!!!

         Tevap=Ttop-dTcw                          ! Evaporator temperature, K
```

```
        q11poreN=(q11chip*L*W)/Aevap            ! Heat flux, necessary to remove heat, W/m2

print*,"q11poreN",q11poreN
print*,"dTcw",dTcw
print*,"dPvapor",dPvapor


print*,"numtot"
print*,numtot

print*,"numl"
print*,numl

print*,"numw"
print*,numw

print*,"d"
print*,d

print*,"h"
print*,h

print*,"b"
print*,b

print*,"p"
print*,p

print*,"W"
print*,W

print*,"p/d"
print*,pdratio

print*,"dPtotmax"
print*,dPtotmax

print*,"dPcap"
print*,dPcap

print*,"dPtotal"
print*,dPtotal

print*,"dPvaptr"
print*,dPvaptr

print*,"dPliqtr"
print*,dPliqtr

print*,"dPliquid"
print*,dPliquid

print*,"dPvapor"
print*,dPvapor

print*,"Paverage"
```

```fortran
      print*,Paverage

      print*,"Tw"
      print*,Tevap

      print*,"dTcw"
      print*,dTcw

      print*,"q11poreR"
      print*,q11poreR

      print*,"q11poreN"
      print*,q11poreN

      print*,"Vlp"
      print*,Vlp

      print*,"Rev"
      print*,Rev

      print*,"Vv"
      print*,Vv

      print*,"mdottot"
      print*,mdottot


10    continue
      stop
      end program evaporator
```

VITA

Alexandre Viktorovich Alexseev was born 18 July 1977 in Kiev, Ukraine. After graduating in 1994 from School #1 in Keperveyem, Bilibino district, Magadan region, Russia, he enrolled in the nuclear engineering program at Obninsk Institute of Nuclear Power Engineering in Obninsk, Kaluga region, Russia. He received a B.S. in April 2000 and, afterwards, worked as an engineer at the Russia State Scientific Center Institute for Physics and Power Engineering, Obninsk, Russia, until 2001. He came to the United States in August 2001 and studied at Texas A&M University, College Station, majoring in nuclear engineering. He received his M.S. in August 2003. He can be reached through the Department of Nuclear Engineering, 129 Zachry, Texas A&M University, College Station, Texas 77843.